Earth-Science Reviews 281 (2026) 105633

Contents lists available at ScienceDirect

Earth-Science Reviews

journal homepage: www.elsevier.com/locate/earscirev

Review Article

Global geometry of mid-ocean and back-arc ridge systems: Ridge segments, transform faults, and non-transform offsets

Javier Escartín[a,*], Benjamin Sautter[b,c], Carmen Gaina[d,e], Roi Granot[f], Sven Petersen[g], Manuel Pubellier[a,c]

[a] Laboratoire de Géologie, UMR 8538, Département de Géosciences, École Normale Supérieure, CNRS, Université PSL, Paris, France
[b] Geo-Ocean, Univ Bretagne Sud, Univ Brest, CNRS, Ifremer, UMR6538, F-56000 Vannes, France
[c] Commission for the Geological Map of the World, Paris, France
[d] Centre for Planetary Habitability (PHAB), Department of Geosciences, University of Oslo, Norway
[e] School of Earth and Planetary Sciences (EPS), Curtin University, Perth, Australia
[f] Deparment of Earth and Environmental Sciences, Ben-Gurion University of the Negev, Beer-Sheva, Israel
[g] GEOMAR Helmholtz Centre for Ocean Research, Kiel, Germany

ARTICLE INFO

Keywords:
Mid-ocean ridges
Ridge segment
Non-transform offsets
Oceanic transform faults
Oceanic lithosphere
Marine tectonics
Ridge offset

ABSTRACT

The total length of the global mid-ocean ridge system length is currently estimated at 50000 to 100000 km. To define in detail the complex structure of divergent plate boundaries, and to accurately evaluate its length and the geometry of ridge offsets, we present the MAPRIDGES database. It provides the first comprehensive global compilation of mid-ocean ridge geometry interpreted from multibeam bathymetry, encompassing in detail individual ridge segments, transform faults, and non-transform offsets (NTOs). The database includes 262 transform faults and 10 transform zones, totalling ~28.000 km. We quantify for the first time both overlapping and underlapping NTOs at divergent plate boundaries and find a cumulative lateral offset of ~9.000 km, representing one-third of the cumulative length of transform offsets. The database incorporates 1471 ridge segments reaching a total length of ~71200 km, while the global ridge length corrected for NTOs overlaps and underlaps amounts to ~67900 km.

Mid-ocean ridge spreading rate exerts a first-order control on the geometry and nature of mid-ocean ridge segmentation. We document that at rates below a spreading rate threshold of ~80-100 mm/yr, the proportion of overlapping NTOs increases with spreading rate, while the cumulative lateral offset decreases. At rates above this spreading rate threshold there is no apparent dependence of NTOs geometry on spreading rate. We also document that the lateral offset of NTOs and transforms show a significant overlap, with numerous transforms displaying offset lengths below 40 km, and NTOs exceeding 50 km. NTOs affect about 10% of the oceanic crust along-axis, reshaping the lithosphere with tectonic deformation, volcanism, hydrothermal activity and alteration. Consequently, these non-transform discontinuities, together with transform faults, should be systematically included in global assessments of lithospheric accretion, alteration, and associated fluxes of fluids and elements at mid-ocean ridges. We suggest that ridge segmentation and the nature of discontinuities are influenced by multiple factors beyond spreading rate, including mantle temperature, melt supply, and ridge obliquity, in addition to local intra- and inter-segment variability. Analyses of the patterns reported here might help understanding the nature and evolution of magmatic vs. tectonic-dominated ridge segments and their terminations.

Contents

* Corresponding author.
E-mail address: escartin@geologie.ens.fr (J. Escartín).

https://doi.org/10.1016/j.earscirev.2026.105633
Received 29 April 2026; Received in revised form 17 July 2026; Accepted 19 July 2026
Available online 29 July 2026
0012-8252/

1. Introduction

Oceanic basins formed at mid-oceanic ridges account for ~70% of the Earth's lithosphere. These divergent plate boundaries accommodate plate separation over a narrow and well-defined band of oceanic lithosphere, that facilitates its identification and mapping [e.g., Gordon, 1998]. The length of the global ridge system has been estimated at 50000 to 100000 km approximately (Table 1), depending on the geometry of divergent plate boundary geometry considered (e.g., taking into account only ridge segments, or including transform faults and other discontinuities in the calculation), and data quality or methods used in these different studies [Menard, 1961; Macdonald et al., 1991; Baker et al., 1996; Bird, 2003; Müller et al., 2013; Gale et al., 2014; Cogné and Humler, 2004; Cao et al., 2024].

The composition and structure of the oceanic lithosphere depend on the interactions between magma supply and tectonic extension at the ridge axis. These interactions are also modulated by cooling through seawater circulation, associated alteration of the lithosphere, and the resulting chemical exchanges with the overlying ocean. There are thus complex feedbacks between melt supply, tectonic deformation, cooling, and thermal structure of the lithosphere beneath the ridge axis. As a result, spreading rate and melt supply at the axis are important but not the sole parameters controlling the nature and structure of the ridge axis.

Table 1
Estimates of the total length of the global ridge system or divergent plate boundaries.

Reference	Length, km	Note
Menard [1961]	~64000 (40000 mi)	No method specified
Macdonald et al. [1991]	~70000	No method specified
Baker et al. [1996]	58600	Divergent boundaries with Pacific back-arcs
Bird [2003]	67338	Ridges
	47783[a]	Transform faults, including plate boundaries
Müller et al. [2013]	70000	No method specified
Gale et al. [2014]	60864	Total length of 771 ridge segments
Cogné and Humler, 2004	51747	Distances along meridians of rotation poles
Hasterok et al. [2022]	99664[b]	Spreading centers (including transform faults)
	99894[b]	Length of transform plate boundaries (all)
Cao et al. [2024]	~95000*	Ridges and transforms (from Fig. 15)

[a] The length of transform faults reported by Bird [2003] includes in some cases non-transform offsets (e.g., along the East-Pacific Rise, Fig. 14).
[b] The plate boundary lengths include ridge segments and transform faults.

Mid-ocean ridges consist of ridge segments which may be offset by transform faults or disrupted by other type of discontinuities, including non-transform offsets. Ridge segments can be considered as the elementary unit of oceanic lithospheric formation, with segment lengths typically ranging between ~30 and 100 km [e.g., Macdonald, 1982; Sempéré et al., 1990a]. In this study we refer to 'accretion of oceanic lithosphere' to encompass both magmatically continuous oceanic lithosphere, and a heterogeneous one. Different modes of accretion of the oceanic lithosphere are observed at ridge axes. These range from almost exclusively magmatic accretion, to tectonic extension associated with detachment faulting, and the emplacement of mantle rocks in the lithosphere and their exposure at the seafloor [e.g., Cannat et al., 2006; Olive and Dublanchet, 2020]. These accretion modes can be identified from seafloor morphology, which serves as a record of magmatic and tectonic interactions occurring at the ridge axis [Escartín and Olive, 2022; Tucholke et al., 2023]. Along ridges with robust magma supply, the produced lithosphere displays closely-spaced, ridge-parallel, and fault-bounded abyssal hills [Kappel and Ryan, 1986; Macdonald et al., 1996; Olive et al., 2015]. When tectonic activity dominates, the seafloor displays instead a variety of morphologies, including irregularly distributed massifs [e.g., Smith et al., 2006; Cann et al., 2015] or broad smooth mounds (e.g., 'smooth seafloor' [Cannat et al., 2006]), controlled by long-lived normal faulting (oceanic detachments). Along ridge sections with reduced melt supply, the resulting axial lithosphere includes both mantle material and magmatic rocks [Cannat et al., 1995].

Accretion processes along mid-ocean and back-arc ridge axes are thus discontinuous, but organized at different spatial scales by transform faults and ridge segments. Transform faults efficiently localize along strike-slip faults and are thus relatively stable and often long-lived. At non-transform offsets (NTOs) the relative motion of the adjacent plates is distributed, and the discontinuity may migrate along-axis over time [e.g., Spencer et al., 1997; Harper et al., 2023]. Early models have attributed this segmentation to discontinuous melt supply along the ridge axis [e.g., Whitehead et al., 1984; Kuo and Forsyth, 1988; Lin et al., 1990], or to tectonic discontinuities and deformation processes in the brittle lithosphere [Mutter and Karson, 1992].

While transform faults are often perceived as merely tectonic features, recent studies show that these structures are active, and host diking and volcanism, off-axis tectonic deformation, and fluid flow with hydration of the underlying mantle [e.g., McGuire et al., 2012; Bonatti et al., 2005; Hensen et al., 2019; Prigent et al., 2020; Thomas et al., 2022; Chesley et al., 2025], among other processes. As a result, active transforms contribute to global chemical fluxes linked to the oceanic lithosphere (e.g., alteration [e.g., Rüpke and Hasenclever, 2017]) and add to the contribution associated with mid-ocean ridges. For this quantification, both the distribution and geometry of transform faults, while relatively well established [e.g., Wolfson-Schwehr and Boettcher, 2019; Ren et al., 2022], does require a revision based on recent bathymetry data and their re-interpretation.

Non-transform offsets, as in the case of transforms, host processes such as alteration, deformation and magmatism [Hey, 1977; Gràcia et al., 2000; Wetzel et al., 1993; Tyler et al., 2007] that also modify the lithosphere and contribute to the fluxes mentioned above. To date, there is no quantification nor global evaluation of their impact, nor of their relative importance with respect to oceanic transform faults. This is in part owing to the lack of a systematic mapping and characterization of the geometry of the ridge axis and associated NTOs. This mapping is required to quantify the length of axis and the amount of oceanic lithosphere impacted by alteration, deformation, or volcanism at NTOs. Since available studies quantifying the heat and chemical fluxes linked to mid-ocean ridges [e.g., Alt, 2003; Baker, 2007] are based primarily on processes along the ridge axis, there is room for improvement by considering the entire mid-ocean ridge boundary, including NTOs and transform offsets.

Initiatives to map mid-ocean ridge segments and associated transform faults began as part of establishing the plate tectonics theory and shortly after that for identifying the structure and role of plate boundaries in global tectonics [Ewing and Heezen, 2013; Menard, 1965; Menard and Atwater, 1969; Menard and Atwater, 1969]. Studies interested in global kinematics and evolution of oceanic lithosphere consider plate boundary geometry in the context of their geological history, combining bathymetry with various other geophysical data (gravity, magnetic anomalies). One of the first global maps documenting present and past oceanic plate boundaries, together with isochrons defining oceanic crust age, was published by Pitman et al. [1974]. The first digitally available compilation of oceanic isochrons, which are past and present plate boundaries (mid-ocean ridges, oceanic transform faults and trenches) by Müller et al. [1997] relied on marine gravity data from the GEOSAT Exact Repeat Mission, Geodetic Mission, and ERS1 satellite altimetry [Sandwell, 1986], bathymetric data, and earthquake epicentres. Global isochron maps including active mid-ocean ridges were continuously updated [Müller et al., 2008; Seton et al., 2012; Müller et al., 2019) and incorporated in the GPlates application (https://www.gplates.org). This included minor adjustments to the location of ridge segments and transform faults, based on improved bathymetry and gravity models. Although these models and the ocean crust age grids were used for numerous global studies, a quantification of the present-day oceanic plate boundary geometry and length was not specifically included in their publications. Lately, Hasterok et al. [2022] refined the GPlates mid-ocean ridge local geometry while calculating the lengths spreading centres and transforms (Table 1).

The widely used global plate boundary model PB2002 [Bird, 2003], applied minor edits to the boundaries initiated by the Paleo-Oceanographic Mapping Project at the University of Texas [Müller et al., 1997]. It was ensured that the active plate boundaries met at triple-junction points, which are common to all digitized boundary segments, and the non-transform offsets on spreading ridges were replaced with idealized transforms. The PB2002 model was among the first to quantify separately the number of mid-ocean ridge and transform fault segments (Table 1).

Studies dedicated to detailed mid-ocean morphology, like Macdonald et al. [1991] and similar publications, paid attention to present-day plate boundary segmentation and proposed a hierarchical classification of ridge segments and the associated discontinuities based on detailed morphology. The definition of divergent plate boundaries and their associated segmentation used available bathymetric maps, combined with the distribution of earthquakes, and magnetic data. The

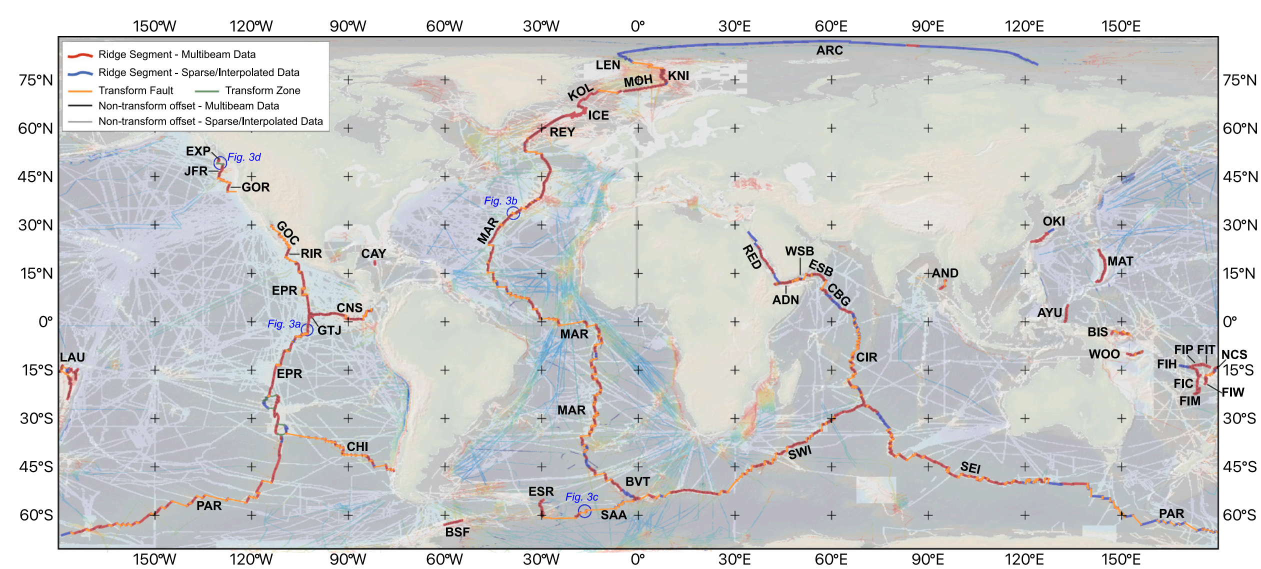

Fig. 1. Map showing the geometry of the global mid-ocean ridge system, with associated transforms and non-transform offsets from the MAPRIDGES database (See Supplementary Materials for a detailed description of the database). Names of ridges: ADN: Gulf of Aden; AND: Andaman Sea; ARC: Arctic Ridges; AYU: Ayu Trough; BIS: Bismarck Sea; BSF: Bransfield Strait; BVT: Bouvet Triple Junction; CAY: Cayman Ridge; CBG: Carlsberg Ridge; CHI: Chile Ridge; CIR: Central Indian Ridge; CNS: Cocos-Nazca Spreading Center; EPR: East Pacific Rise; ESB: East Sheba Ridge; EXP: Explorer Ridge; FIC: Fiji Central Spreading Ridge; FIH: Fiji Hazel Holme Ridge; FIM: Fiji Monzier Rift; FIP: Fiji South Pandora Ridge; FIT: Fiji Tripartite Ridge; FIW: Fiji Western Ridge; GOC: Gulf of California; GOR: Gorda Ridge; GTJ: Galapagos Triple Junction; ICE: Iceland Ridge (subaerial); JFR: Juan de Fuca Ridge; KNI: Knipovich Ridge; KOL: Kolbeinsey Ridge; LAU: Lau Basin; LEN: Lena Trough; MAR: Mid-Atlantic Ridge; MAT: Mariana Trough; MOH: Mohns ridge; NCS: North Cikobia Spreading Center; OKI: Okinawa Trough; PAR: Pacific Antarctic Ridge; RED: Red Sea Ridge; REY: Reykjanes Ridge; RIR: Rivera Rise; SAA: South American - Antarctic Ridge; SEI: South-East Indian Ridge; SWI: Southwest Indian Ridge; WSR: West Sheba Ridge; WOO: Woodlark Basin. The background shows the GMRT data and overlays of the NCEI-IHO, OBDC and DAM bathymetry data (last accessed January 2025) emphasizing significant regional variations in multibeam coverage and data gaps. An A0 version of the basemap is available in Supplementary Materials Fig. S1. Blue circles locate panels in Fig. 3.

resulting plate boundary identifications and their associated segmentation [e.g., Bird, 2003], have served as a basis for a better understanding of trends in the mid-ocean ridge petrology and geochemistry and potential links to mantle temperature underlying the ridge axis [e.g., Klein and Langmuir, 1987; Gale et al., 2014; Dalton et al., 2014].

While only 25% of the global ocean seafloor is imaged by multibeam bathymetry (https://seabed2030.org), mid-ocean ridges are much better covered, with more than 75% of these regions surveyed during decades of research focused on ridge processes. Exploiting globally available, shipboard multibeam bathymetry data from different sources we systematically map in detail ridge segments and associated discontinuities, while providing the most complete and up-to-date catalogue of transform faults. Using these data, we estimate the overall length of the plate boundary associated with mid-ocean ridges and back arc systems, quantify the relative importance of transforms, NTOs, and ridge axis segments (Fig. 1), and establish their distribution as a function of spreading rate. This first quantification of the geometry of non-transform offsets (lateral and along-axis offset) demonstrates the important role of NTOs in oceanic accretion. Our ridge system dataset is compiled as a publicly available database (MAPRIDGESv2602, Sautter et al. [2024]) that can further facilitate studies of ocean ridge processes (e.g., seismicity, magmatic and chemical budgets), and evaluate controlling parameters controlling lithospheric accretion (spreading rate, magma supply, obliquity, tectonic and hydrothermal activity, etc.).

2. Defining the mid-ocean ridge geometry globally: data, methodology and database

Although considered a continuous plate boundary, the ridge system is disjointed, displaying discontinuities with associated lateral offsets that limit individual ridge segment along the ridge axis. These segments can be considered as the quantum of oceanic accretion through a combination of magmatic and tectonic processes, and linked to hydrothermal circulation and lithospheric alteration. Through these processes, the seafloor morphology records the history of past tectonic, magmatic, and hydrothermal interactions, and their impact on ridge segmentation [e.g., Goff, 2020; Roth et al., 2019; Tucholke et al., 2023].

Our study has three main objectives: a) to establish the geometry of individual ridge segments; b) to provide the most complete catalogue of transform faults, large-offset transform zones (lacking localized deformation as found along transform faults), and non-transform offsets; and c) to quantify parameters of the global mid-ocean ridge system, including ridge length, lateral offset of both NTOs and transform faults, along-axis overlap, and the distribution as a function of spreading rate.

2.1. Data

Available modern ship-based bathymetry provides adequate coverage along more than 75% of the global mid-ocean ridges system, and at a sufficient resolution (~50-100 m per pixel), to define the global segmentation of mid-ocean ridges. The mapping of the ridge axis presented here (Fig. 1) relies on publicly available global bathymetry compilations, including the Global Multi-Resolution Topography (GMRT, https://www.gmrt.org/) [Ryan et al., 2009], the National Center for Environmental Information and the IHO Data Center for Digital Bathymetry (NCEI-IHO DCB, https://www.ncei.noaa.gov/maps/bathymetry/), the German Marine Research Alliance (DAM) portal (https://marine-data.de/about), the IBCAO circum-Arctic compilation [Jakobsson et al., 2024], and the Australian AusSeaBed alliance (https://portal.ga.gov.au/persona/marine). These databases offer various Web Map Services (WMS) to visualize the multibeam bathymetry and seafloor morphology at their highest resolution (~100 m or better). GMRT also provides predicted bathymetry, derived from satellite altimetry, in areas lacking multibeam data (see Sandwell and Smith [1997]). This allows us to define the ridge axis in areas lacking multibeam bathymetry, albeit with uncertainties in the location and detailed geometry of the ridge, as described in detail below. The global GEBCO bathymetry compilation (GEBCO, 2024) includes data that is not available in the abovementioned datasets, but its resolution of 15 arcsec (~460m along meridians) makes it unsuitable for a detailed mapping of individual ridge segments and associated discontinuities.

To complement these publicly available global datasets, we collected bathymetry grids from various data repositories (e.g., pangaea.de, seanoe.org, zenodo.org), from scientific journals and their associated digital resources, and from datasets provided to the authors. We also georeferenced published maps extracted from articles where digital data were unavailable. These include bathymetric and acoustic backscatter data, as well as detailed geological and tectonic interpretations based on shipboard data. Mid-ocean ridge sections lacking bathymetry from the sources listed above are digitized based on satellite-derived bathymetry, which is included in the GMRT data products filling gaps between multibeam surveys. All data sources are integrated into a GIS project for visualization at appropriate scales. The MAPRIDGES database includes the geometry of ridge segments, transform faults and zones, and non-transform offsets (Fig. 1 and Fig. S1), described below, and a set of continuous divergent plate boundary sections linking adjacent ridge segments (Fig. S2). These features are also associated with other text attributes (e.g., names, ridge system etc.), described in the Supplementary materials.

2.1.1. Identification of the main components of mid-ocean ridge geometry

A mid-ocean ridge is an assembly of ridge segments, that accommodate the extensional motion between two tectonic plates, and their connectors, which can be transform faults, or non-transform regions. Transform faults are, to a first order, parallel to the spreading direction and follow small circles of the pole of rotation between adjacent plates (Fig. 2a). The lateral offset of transform faults can thus be approximated by the transform length between the two ridge segment end points, with no along-axis offset (Fig. 2a). Non-transform offsets (NTOs) display instead distributed deformation in the absence of a well-defined transform fault, and show two main geometries (Fig. 2b, c). Adjacent segments may exhibit either an along-axis gap (Fig. 2b) or may overlap instead (e.g., overlapping spreading centres, a geometry common at fast-spreading ridges [Macdonald and Fox, 1983], Fig. 2). Fig. 2 illustrates how the along-axis offset (AO), and the lateral offset (LO) at non-transform offsets are defined based on the local spreading direction. In our database, the AO values associated with transform faults are negligible; therefore, we consider them to be zero. For overlapping NTOs, LO may vary along-axis, and in this study, we consider the mean lateral offset (LO_{Mean}, Fig. 2b). The amount of oceanic lithosphere impacted by non-transform processes (deformation, alteration, hydrothermal circulation, late magmatic intrusions, etc.) can be constrained from the along-axis and lateral offset (grey zone labelled A in Fig. 2b, c). Ridge segments are terminated by either an NTO or a transform fault, and the total ridge length is calculated cumulatively from the length of individual ridge segments, considering the along-axis underlap and overlap lengths (AO in Fig. 2b, c), as shown in Fig. 2. Transform zones, that correspond to long-offset structures, having lengths comparable to transform faults but lacking localized deformation, are also mapped in this study and described in the next section.

2.2. The MAPRIDGES database

2.2.1. Identification of ridge segments

The MAPRIDGES database includes 1471 digitized ridge segments. Most fast-spreading ridges (Fig. 3a) and some ridge sections with robust melt supply at intermediate to slow-spreading systems are defined by an axial high. In these cases, we follow the axial high along-axis, terminating individual segments at either transform and non-transform discontinuities (e.g., transforms, overlapping spreading centres, or minor offsets or deviations of the axial high or '*devals*' [Macdonald and Fox, 1983]). At ridge sections lacking an axial high (e.g., rift valley at

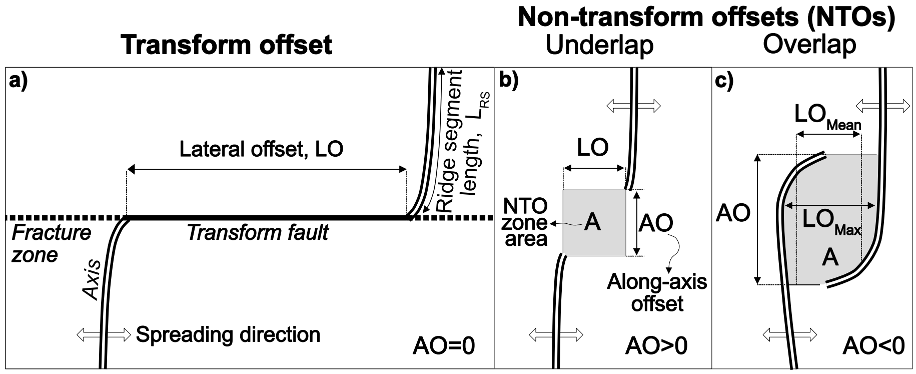

Fig. 2. Geometrical parameters at transform and non-transform offsets (NTOs). a) The lateral offset (LO) at transforms can be approximated by the transform fault length. The tips of adjacent ridge segments align in the spreading direction with no along-axis offsets (AO=0). NTOs can either display a gap along-axis (AO>0, or underlap, b), or an overlap (AO<0) of adjacent segments (c). At underlaps (b), the lateral and along-axis offsets (LO and AO respectively) is the distance between the tip of adjacent segments in the spreading direction for LO, and that perpendicular to spreading for AO. At overlaps, the lateral offset may vary along-axis, depending on overlapping ridge geometry, and can be quantified by the mean or maximum lateral offsets (LO_{Mean} and LO_{Max} respectively). The length of individual ridge segments (L_{RS}) is calculated from the digitized geometry, and NTOs are digitized joining the ends of adjacent segments (see Fig. 3a and b).

slow-spreading ridges), the criteria to position the axis depends on seafloor morphology reflecting tectonic and volcanic structures. The segment axis thus corresponds to the summit of volcanic ridges within the axial rift valley floor, or the mid- or lowest point of the rift floor valley in the absence of clear axial volcanic ridges (Fig. 3b). Segments are terminated at either transforms (Fig. 3a, b) or non-transform offsets, both underlapping (Fig. 3b) or overlapping (Fig. 3a, b). In areas that are poorly mapped or unmapped, the axis of segments runs along the lowest point of the interpolated bathymetry (Fig. 3c), and their termination corresponds to clear offsets of the axis that can often be traced off-axis as fracture zones or the wake of NTOs, which show along-axis migration. For the subaerial portion of the Mid-Atlantic Ridge in Iceland (ICE in Fig. 1) we followed the volcanic segments as provided by the Iceland Geosurvey ISOR (web access: https://arcgisserver.isor.is). Volcanic segments in Iceland show significant lateral overlap and discontinuity along axis, with an overall geometry and segment morphology that differ significantly from that of the remaining submarine ridge system.

We appraise the uncertainty on digitization as a degree of confidence of 1 (low confidence) or 2 (high confidence). A confidence of 1 is assigned to a ridge segment if the region is only mapped with interpolated bathymetry or of low resolution (>200m). A confidence of 2 refers to regions mapped with multibeam bathymetry, associated backscatter and/or associated published studies. Of the 1471 segments in the MAPRIGES database, less than 15% are flagged as 'poorly or unmapped', while the remaining have sufficient bathymetry coverage to adequately constrain the location and geometry of the ridge segment axis.

We identify several additional segment mapping uncertainties. First, in tectonically complex areas, segmentation is ill-defined in the seafloor morphology, and ridge segments may be subject to alternative interpretations. This is the case of the Arctic and portions of the Red Sea ridges (Fig. 1, labelled ARC and RED respectively; see Fig. S3 for a section of the Red Sea [Augustin et al., 2016]), which display a continuous rift valley with no clear lateral offsets, or partial sediment cover masking the detailed morphology of the oceanic crust; these uncertainties are independent of bathymetric coverage. In the case of the Red Sea, the axial morphology and geometry of the ridge, as well as its sedimented nature is revealed by recent multibeam surveys [Augustin et al., 2016]. Geophysical basement imaging, however, suggests that sections of the mid-ocean ridge are associated with an axial high that is obscured by sedimentation [Shi et al., 2018]. Second, in areas lacking multibeam bathymetry, NTOs may not be identifiable, and the segments in the MAPRIDGES database may instead correspond to several segments and associated NTOs. Finally, MAPRIDGES is based on a visual interpretation and manual digitization, with a validation by co-authors, that remains subjective. The number of segments will likely increase with the availability of new bathymetry over unmapped areas, that are a relatively small fraction of the total ridge system (<25%). These improvements and corrections will not change the main conclusions of our work, as they may modify the overall length of the ridge system only marginally, while modestly increasing the number of NTOs and their cumulative along-axis and lateral offsets.

2.2.2. *Transform faults*

Transform faults link ridge segments that are adjacent along-axis with a well-defined, localized strike-slip movement (Fig. 3a, b). Multibeam bathymetry data of adequate resolution may reveal the traces of recent, active strike-slip faults, identifiable along part of the transform fault, and in some cases, linking the ends of adjacent ridge segments. At other well-surveyed transforms, our interpretation follows features such as median ridges within transform valleys, the trough left by strike-slip fault valleys, or traces of recent strike-slip fault activity. In partially mapped or unmapped transform faults, we use satellite-derived bathymetry (GMRT dataset) and follow the transform trough along its deepest point. The offset associated with transform faults corresponds to the length of its trace.

The MAPRIDGES database reveals that in many cases transform fault traces are complex, show varying structure and strands at local scales (~10 km), and a geometry that suggests a complex tectonic structure and accommodation of strike-slip deformation. These aspects are not considered in this paper which focuses on providing a first detailed and global mapping of these structures, and the quantification of basic geometrical parameters along the global mid-ocean ridge system.

2.2.3. *Transform zones*

Transform zones are large-offset linear structures that do not exhibit a well-defined zone of localized deformation, such as the Sovanco Fracture Zone [Cowan et al., 1986] Fig. 3d). Some transform zones exhibit distributed deformation and may be associated with either transpression [e.g., Bird, 2003] or transtension across their traces, resulting from changes in the relative motion of tectonic plates. For these structures we have digitized a trace following the zone of most apparent deformation. While their distributed deformation may be comparable to that of NTOs, their lateral offset (exceeding 200 km) is significantly longer than those of NTOs. As for transform faults, the lateral offset (LO) associated with transform zones corresponds to the total length of their trace, with an along-axis offset (AO) assumed to be zero (Fig. 2a).

Following the above-mentioned methodology, we provide the most complete catalogue of transform faults associated with the global mid-ocean ridge system, accounting for 262 transform faults, and 10

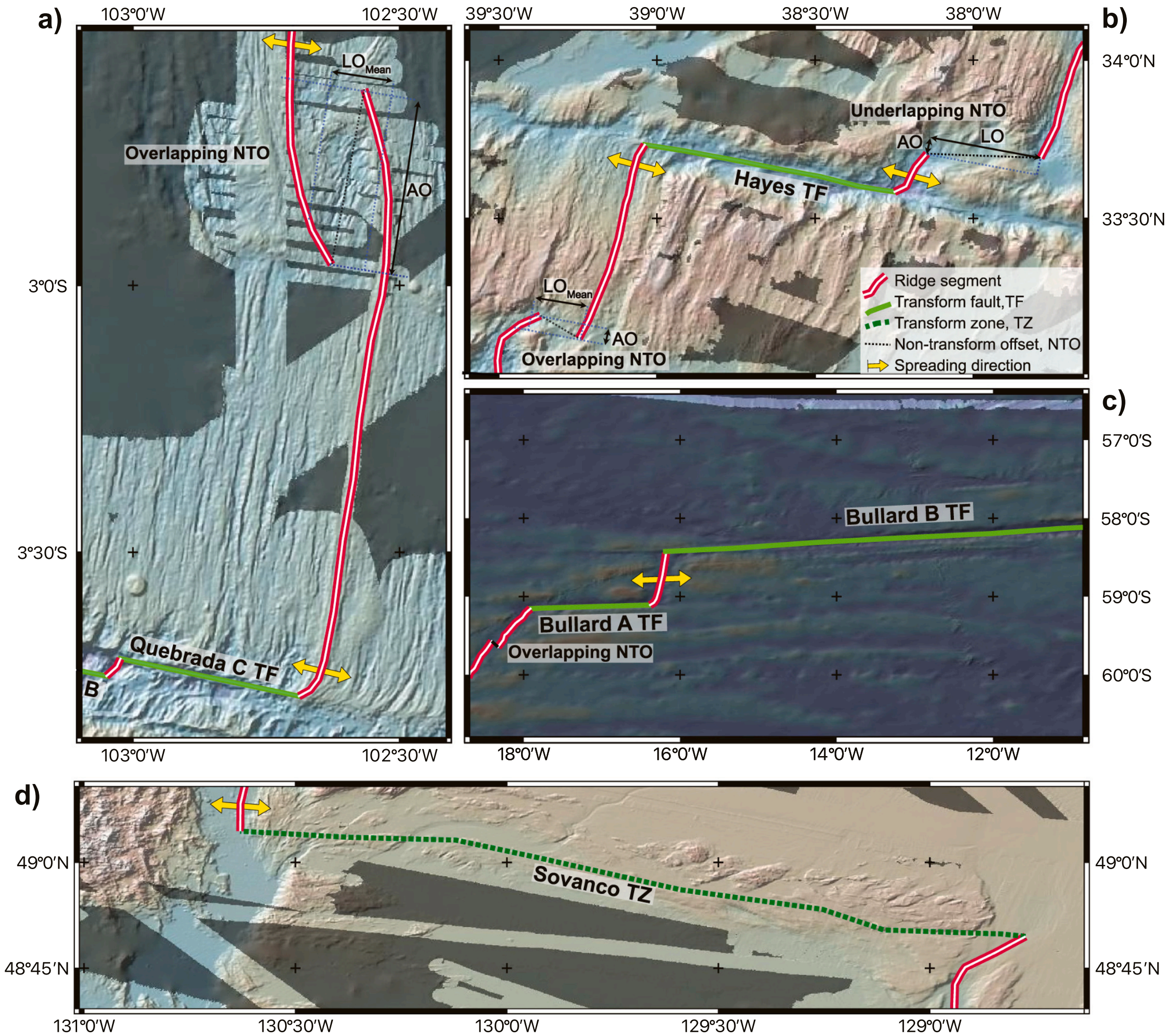

Fig. 3. Examples of transform faults (TFs) and overlapping and underlapping non-transform offsets (NTOs). a) Overlapping NTO along the fast-spreading East Pacific Rise, N of the Quebrada TF complex. b) Ridge segments along the slow-spreading Northern Mid-Atlantic Ridge showing underlapping and overlapping NTOs North and South of the Hayes TF respectively. In a) and b ridge segments and geometry of discontinuities (dashed black lines linking segment ends for NTOs) are digitized from multibeam bathymetry. c) Ridge segments, NTO and TFs in a region of the lobal mid-ocean ridge system lacking multibeam bathymetry, and where satellite-derived bathymetry data (background filling multibeam data gaps in the GMRT bathymetry data) were used for their mapping. d) Example of the Sovanco transform zone, showing distributed deformation. Location of each panel is shown by blue circles in Fig. 1.

transform zones. Our study excludes strike-slip plate boundaries or major features (e.g., Shackleton Fracture Zone between the Scotia and Antarctic Plates) not linked to ridge segments. Table 2 also groups the closely spaced transform faults that compose multi-transform systems [e.g., Searle, 1983]. We have exhaustively revised the naming of these features, based on a thorough review of literature and published maps. To facilitate the identification of unnamed features, we assigned coded names based on the ridge system in which they are located and a latitude or longitude value approximately corresponding to the centre point of the transform (see the metadata description in Supplementary Materials). A synthesis of transform fault parameters including name, length, and estimated offset age from age grids [Seton et al., 2020] is given in Table 2, and Supplementary Materials Table 3 presenting additional parameters. This also includes reference information on transform faults provided by prior compilations [Wolfson-Schwehr and Boettcher, 2019; Ren et al., 2022].

2.2.4. *Non-transform offsets*

NTOs are characterized by zones of distributed strike-slip deformation, lacking a clear, localized transform fault as described above (Figs. 2b-c and 3). At slow-spreading ridges, NTOs often show underlaps (see Fig. 2) with a wide range of morphologies, depending on ridge obliquity, melt supply to the axis, style of tectonic deformation (e.g., presence or absence of detachment faults). These structures may also be inherited from the geometry of rift-initiation [e.g., Taylor, 1979; Taylor et al., 1999] and are recognizable at young ocean basins such as the Red Sea and Gulf of Aden [Bellahsen et al., 2013; Izzeldin and Mitchell, 2024]. These may evolve over time, owing to changes in plate motion [e.g., Vogt et al., 1969; Lodolo et al., 2013], to dynamic processes at the axis such as propagation driven by gravity gradients [Harper et al., 2023], readjustments along oblique ridge sections [van Wijk and Blackman, 2007; Su et al., 2026], and in response to changes in accretion and melt supply [e.g., Panasiuk et al., 2025], among other processes. All of these can promote migrations of discontinuities along the ridge axis, or the formation or arrest of stable boundaries (transform

Table 2
List of transform faults along mid-ocean ridges and back-arc spreading systems, and associated parameters (position of transform ends, length in km, adjacent plate names, and age offset). The MAPRIDGES database includes additional information (see details in text and Supplementary Materials Table 1). The age offset reported in this study corresponds to the age of the oceanic lithosphere across each of the ridge-transform intersections, and based on the Seton et al. [2020] digital age map (columns **Age#1** and **Age#2**). We also report the age offset in the compilation by Ren et al. [2022] (column **R22**). Complex transforms, showing several adjacent and closely spaced transform faults, are grouped and shaded in grey, with a name assigned to both the group and the individual transform faults, and the cumulative lateral offset length for each complex.

			Ridge-transform intersection				Length	Plates			Age offset		
Index	Name	Type[a]	Lon1	Lat1	Lon2	Lat2	km	Plate#1	Plate#2	Plate#3	Age#1	Age#2	R22
	Chile Rise												
1	Darwin	T. Fault	-76.683	-45.980	-75.986	-45.842	56.0	Marie Bird Land	Nazca		1.1	1.5	1.9
2	Guamblin	T. Fault	-77.873	-45.798	-76.903	-45.626	77.7	Marie Bird Land	Nazca		2.2	2.9	
3	Guafo	T. Fault	-78.367	-44.444	-81.921	-44.997	287.8	Marie Bird Land	Nazca		7.6	8	11.2
4	Chiloe	T. Fault	-82.713	-42.971	-83.395	-43.073	56.7	Marie Bird Land	Nazca		1.7	1.7	2.3
	Valdivia Complex						574.0	Marie Bird Land	Nazca		13.5	14.5	
5	Valdivia G	T. Fault	-84.602	-41.589	-84.360	-41.559	20.4	Marie Bird Land	Nazca		0.5	0.7	1.3
6	Valdivia F	T. Fault	-85.526	-41.532	-84.696	-41.443	69.9	Marie Bird Land	Nazca		2	2.3	2.5
7	Valdivia E	T. Fault	-85.730	-41.304	-87.656	-41.500	162.5	Marie Bird Land	Nazca		4.2	4.7	6.6
8	Valdivia D	T. Fault	-87.767	-41.280	-89.002	-41.374	104.2	Marie Bird Land	Nazca		3.1	3.9	3.9
9	Valdivia C	T. Fault	-89.134	-41.207	-90.288	-41.286	96.9	Marie Bird Land	Nazca		2.3	2.7	1.9
10	Valdivia B	T. Fault	-90.349	-41.172	-91.239	-41.234	74.8	Marie Bird Land	Nazca		1.9	2.1	3.0
11	Valdivia A	T. Fault	-91.287	-41.066	-91.825	-41.108	45.4	Marie Bird Land	Nazca		1.4	1.5	1.9
16	Chile 40S	T. Fault	-91.868	-40.243	-91.583	-40.233	24.2	Marie Bird Land	Nazca		0.9	0.92	0.8
17	Chile 39S	T. Fault	-91.593	-38.951	-92.536	-38.991	81.6	Marie Bird Land	Nazca		2.11	2.29	3.3
	Chile 38S Complex						**101.7**	**Marie Bird Land**	**Nazca**		**2.66**	**2.91**	
18	Chile 38S B	T. Fault	-92.608	-38.394	-93.335	-38.438	63.6	Marie Bird Land	Nazca		N/A	N/A	2.7
19	Chile 38S A	T. Fault	-93.381	-38.337	-93.817	-38.362	38.1	Marie Bird Land	Nazca		N/A	N/A	1.5
	Challenger Complex						**245.5**	**Marie Bird Land**	**Nazca**		**4.7**	**8.4**	
20	Challenger D	T. Fault	-94.107	-37.313	-95.022	-37.333	81.0	Marie Bird Land	Nazca		N/A	N/A	3.3
21	Challenger C	T. Fault	-95.051	-37.252	-95.238	-37.256	16.5	Marie Bird Land	Nazca		N/A	N/A	0.9
22	Challenger B	T. Fault	-95.319	-37.100	-96.104	-37.104	69.8	Marie Bird Land	Nazca		N/A	N/A	2.7
23	Challenger A	T. Fault	-96.166	-37.007	-97.044	-37.005	78.2	Marie Bird Land	Nazca		N/A	N/A	3.2
	Chile complex						**1111.7**				**15.2**		
227	Chile E	T. Fault	-97.953	-36.336	-97.097	-36.315	76.7	Marie Bird Land	Farallon	Nazca	N/A	N/A	
226	Chile D	T. Fault	-99.925	-36.200	-97.953	-36.245	176.9	Marie Bird Land	Farallon		N/A	N/A	
32	Chile C	T. Fault	-102.306	-35.953	-99.928	-35.967	214.0	Marie Bird Land	Farallon		N/A	N/A	
31	Chile B	T. Fault	-104.693	-35.559	-102.302	-35.770	217.2	Marie Bird Land	Farallon		N/A	N/A	
30	Chile A	T. Fault	-109.266	-34.611	-104.686	-35.431	426.9	Marie Bird Land	Farallon		N/A	N/A	
	Galápagos Spreading Centre												
239	GSC 91W	T. Fault	-90.845	1.875	-90.693	1.111	86.6	Nazca	Cocos		1.95	4.2	3.3
27	Inca	T. Fault	-85.368	0.698	-85.272	1.753	118.2	Nazca	Cocos		2.7	5.2	4.1
	Ecuador complex						**163.3**	Nazca	Cocos		**4.5**	5.4	
28	Ecuador A	T. Fault	-84.667	1.746	-84.636	2.199	50.5	Nazca	Cocos		N/A	N/A	
236	Ecuador B	T. Fault	-84.496	2.206	-84.471	2.696	54.6	Nazca	Cocos		N/A	N/A	

(continued on next page)

Table 2 (*continued*)

			Ridge-transform intersection				Length	Plates			Age offset		
Index	Name	Type[a]	Lon1	Lat1	Lon2	Lat2	km	Plate#1	Plate#2	Plate#3	Age#1	Age#2	R22
237	Ecuador C	T. Fault	-84.376	2.703	-84.352	2.904	22.5	Nazca	Cocos		N/A	N/A	
238	Ecuador D	T. Fault	-84.283	2.994	-84.263	3.313	35.7	Nazca	Cocos		N/A	N/A	
72	Panama	T. Fault	-82.920	3.237	-82.909	3.765	58.7	Nazca	Cocos		2	N/A	
	Central Indial Ridge												
109	Gemino	T. Fault	69.146	-22.857	69.423	-22.719	32.2	Africa	India		1.4	1.9	
250	CIR 20.3S	T. Fault	68.032	-20.276	67.765	-20.447	33.7	Africa	India		2.3	2.6	
110	Flinders	T. Fault	67.016	-20.405	67.547	-20.093	65.7	Africa	India		3	3.9	
111	Egeria	T. Fault	66.742	-20.006	66.368	-20.226	46.3	Africa	India		2.3	2.2	
112	Marie Celeste	T. Fault	65.134	-17.984	66.903	-17.025	216.0	Africa	India		10.2	13.2	10.6
113	CIR 16S	T. Fault	66.576	-16.532	67.420	-16.051	104.7	Africa	India		5.7		5.4
114	Argo	T. Fault	65.968	-13.855	66.759	-13.373	100.9	Africa	India		N/A	N/A	
115	CIR 12S	T. Fault	66.411	-11.608	65.629	-12.127	103.0	Africa	India		N/A	N/A	5.7
116	CIR 10S	T. Fault	66.290	-10.320	66.848	-9.918	75.8	Africa	India		N/A	N/A	
117	Vema II	T. Fault	66.633	-9.622	68.264	-8.249	235.4	Africa	India		N/A	N/A	
118	CIR 7S	T. Fault	67.885	-7.801	68.292	-7.421	61.8	Africa	India		N/A	N/A	
119	CIR 6S	T. Fault	67.914	-7.100	68.525	-6.551	90.9	Africa	India		5.1	N/A	
120	Vityaz	T. Fault	68.004	-6.045	68.710	-5.360	109.1	Africa	India		4.9	7.1	
121	CIR 5S	T. Fault	68.448	-4.921	68.736	-4.614	46.7	Africa	India		3	5	
122	Sealark	T. Fault	68.303	-4.093	68.658	-3.670	61.4	Africa	India		3.7	5.3	
123	Mabahiss	T. Fault	68.210	-2.896	67.968	-3.178	41.3	Africa	India		3.7	2.6	
124	CIR 2.5S	T. Fault	68.351	-2.251	67.972	-2.712	66.3	Africa	India		3.5	3.2	
125	CIR 1S	T. Fault	67.401	-1.394	67.674	-0.992	54.1	Africa	India		3.2	3.2	
126	CIR 0.5N	T. Fault	66.936	0.283	67.371	0.904	84.4	Africa	India		4.5	6.4	
127	Owen	T. Fault	56.760	10.172	58.294	12.614	325.2	Africa	India	Arabia			
	Gulf of Aden - Red Sea												
251	Socotra	T. Fault	53.909	14.639	53.759	14.290	42.1	Somalia	Arabia		5.1	4.2	
128	Alula Fartak	T. Fault	52.162	14.726	51.263	13.156	200.0	Somalia	Arabia		18.2	18.5	
129	Mosaso Hami	T. Fault	49.517	13.002	49.683	13.414	49.4	Somalia	Arabia		3.7	5.3	
131	GoA 49.3E	T. Fault	49.257	12.887	49.353	13.061	22.1	Somalia	Arabia		2.5	2.4	
130	Xiis Al Mukalla	T. Fault	48.742	12.806	48.827	13.041	28.0	Somalia	Arabia		2.8	3.4	
252	GoA 48.6E	T. Fault	48.659	12.829	48.611	12.737	11.5	Somalia	Arabia		1.7	N/A	
253	GoA 48E	T. Fault	48.067	12.718	47.931	12.456	32.7	Somalia	Arabia		3.2	5.4	
254	Maskali	T. Fault	43.235	11.867	43.082	11.740	21.9	Denali			N/A	N/A	
255	GoA 43E	T. Fault	43.053	11.752	43.006	11.718	6.4	Denali			N/A	N/A	
	South American - Antarctic Ridge												
207	South Sandwich	T. Fault	-19.456	-60.795	-29.295	-60.693	537.7	South America	Antarctica		>20	N/A	
206	Bullard A	T. Fault	-16.383	-59.108	-17.913	-59.155	87.4	South America	Antarctica		1.8	7	

(*continued on next page*)

Table 2 (*continued*)

			Ridge-transform intersection				Length	Plates			Age offset		
Index	Name	Type[a]	Lon1	Lat1	Lon2	Lat2	km	Plate#1	Plate#2	Plate#3	Age#1	Age#2	R22
202	Bullard B	T. Fault	-16.179	-58.443	-6.984	-57.919	542.4	South America	Antarctica		21.5	22.7	
203	SAAR 57.3S	T. Fault	-7.090	-57.453	-6.089	-57.307	62.1	South America	Antarctica		7.3	7.1	
204	SAAR 56.6S	T. Fault	-6.241	-56.706	-5.154	-56.605	67.6	South America	Antarctica		4.7	6.1	
205	SAAR 56.3S	T. Fault	-5.195	-56.350	-4.691	-56.290	31.7	South America	Antarctica		3.9	3.3	
201	Conrad	T. Fault	-1.598	-55.636	-4.777	-55.755	199.7	South America	Antarctica		N/A	17.5	
	Mid-Atlantic Ridge												
151	MAR 50S	T. Fault	-9.823	-49.287	-8.480	-48.955	104.4	South America	Africa		10.4	6.1	
152	Falkland	T. Fault	-10.540	-46.968	-13.364	-47.563	223.6	South America	Africa		11.6	12.6	15.3
153	MAR 40S	T. Fault	-16.850	-40.426	-16.448	-40.293	37.2	South America	Africa		2	2.4	
154	Gough	T. Fault	-16.573	-39.855	-15.921	-39.712	58.0	South America	Africa		2.7	3.1	
155	Tristan da Cunha	T. Fault	-16.392	-38.324	-17.044	-38.433	58.1	South America	Africa		2.7	2.9	
156	Montevideo	T. Fault	-17.793	-35.567	-15.030	-35.200	253.8	South America	Africa		11.7	12.4	
157	Meteor	T. Fault	-15.164	-34.222	-14.499	-34.116	62.4	South America	Africa		3.2	4.1	4.4
	Cox complex						**112.4**	South America	Africa		**6.7**	6.3	
158	Cox A	T. Fault	-14.525	-32.497	-14.294	-32.441	22.5	South America	Africa		N/A	N/A	3.7
159	Cox B	T. Fault	-14.276	-32.323	-13.662	-32.217	58.9	South America	Africa		N/A	N/A	2.0
160	Cox C	T. Fault	-13.634	-32.156	-13.311	-32.103	31.0	South America	Africa		N/A	N/A	
161	MAR 29.75S	T. Fault	-13.867	-29.779	-13.635	-29.744	22.7	South America	Africa		1.17	1.02	1.6
162	MAR 29.2S	T. Fault	-13.780	-29.240	-13.071	-29.132	69.8	South America	Africa		5.1	4.2	
163	MAR 28.9S	T. Fault	-13.104	-28.921	-12.451	-28.812	64.7	South America	Africa		3.2	N/A	3.3
164	MAR 28.2S	T. Fault	-12.665	-28.167	-13.158	-28.284	50.0	South America	Africa		2.8	2.7	3.3
240	Rio Grande	T. Fault	-13.903	-25.695	-13.591	-25.629	32.2	South America	Africa		1.9	2.2	2.3
218	MAR 25S	T. Fault	-13.712	-24.904	-13.357	-24.852	36.5	South America	Africa		2.3	2.1	2.7
	Rio de Janeiro complex						**166.1**	South America	Africa		**10.5**	11	
165	Rio de Janeiro A	T. Fault	-13.631	-22.893	-12.805	-22.731	86.7	South America	Africa		5.2	5.4	5.7
166	Rio de Janeiro B	T. Fault	-12.753	-22.378	-11.998	-22.230	79.4	South America	Africa		6.1	5	5.5
167	MAR 21S	T. Fault	-11.844	-21.262	-11.537	-21.149	34.2	South America	Africa		2	2.2	
168	MAR 18S	T. Fault	-12.973	-17.637	-13.723	-17.841	82.5	South America	Africa		4.7	5	
169	Tetyaev	T. Fault	-14.243	-16.371	-13.172	-16.161	116.8	South America	Africa		6.3	6.9	
170	Cardno	T. Fault	-13.855	-14.035	-14.360	-14.176	56.7	South America	Africa		3.5	4.1	
	Bode Verde complex						**216.4**	South America	Africa		**10.9**	11.9	
171	Bode Verde A	T. Fault	-14.788	-12.313	-14.338	-12.173	51.3	South America	Africa		3.1	3.6	
172	Bode Verde B	T. Fault	-14.405	-11.813	-12.925	-11.492	165.1	South America	Africa		7.8	8.9	
	Ascension complex						**246.4**	South America	Africa		**12.8**	15.2	
173	Ascension A	T. Fault	-13.463	-7.426	-13.018	-7.318	50.7	South America	Africa		N/A	3.9	3.1
174	Ascension B	T. Fault	-12.985	-7.072	-11.257	-6.678	195.6	South America	Africa		10.3	N/A	12.6
175	MAR 5S	T. Fault	-11.609	-4.939	-12.231	-5.114	71.6	South America	Africa		3.4	3.6	5.0

(*continued on next page*)

Table 2 (*continued*)

			Ridge-transform intersection				Length	Plates			Age offset		
Index	Name	Type[a]	Lon1	Lat1	Lon2	Lat2	km	Plate#1	Plate#2	Plate#3	Age#1	Age#2	R22
176	MAR 4S	T. Fault	-12.287	-4.023	-12.058	-3.924	27.7	South America	Africa		1.6	1.9	
241	Chain	T. Fault	-13.146	-0.893	-15.814	-1.581	306.6	South America	Africa		17.5	14	20.9
177	Romanche	T. Fault	-17.041	0.104	-24.612	-1.152	853.9	South America	North-West Africa	Africa	47.2	42.2	58.0
	Saint Paul complex						**584.7**	South America	Africa		**31.8**	28.5	
178	Saint Paul D	T. Fault	-24.985	0.651	-25.459	0.570	53.5	South America	North-West Africa		3.6	5	3.7
179	Saint Paul C	T. Fault	-25.497	0.774	-26.310	0.664	91.3	South America	North-West Africa		9.2	5.4	6.1
180	Saint Paul B	T. Fault	-26.397	0.945	-27.654	0.804	140.6	South America	North-West Africa		3.9	N/A	9.9
181	Saint Paul A	T. Fault	-30.376	0.777	-27.702	1.064	299.3	South America	North-West Africa		13.9	13.6	21.2
183	Strakhov	T. Fault	-31.549	3.960	-32.566	3.901	113.0	South America	North-West Africa		8.3	12.1	8.0
	Dlodrums complex						**722.2**	South America	Africa		**35**	**41**	
219	Bogdanov (Doldrums E)	T. Fault	-34.570	7.146	-33.916	7.194	72.4	South America	North-West Africa		N/A	11	
184	MAR 7.4N (Doldrums D)	T. Fault	-34.724	7.433	-35.999	7.381	140.8	South America	North-West Africa		5.2	N/A	
225	Puscharovky	T. Fault	-36.690	7.473	-36.027	7.511	73.3	South America	North-West Africa		N/A	N/A	
185	Vernadsky (Doldrums C)	T. Fault	-36.710	7.717	-38.033	7.715	145.7	South America	North-West Africa		9.3	10.3	
186	Doldrums (Doldrums B)	T. Fault	-38.025	8.214	-39.603	8.188	173.8	South America	North-West Africa		13.4	11.1	
187	Arkanglesky (Doldrums A)	T. Fault	-39.464	8.814	-40.521	8.829	116.2	South America	North-West Africa		6.1	8.1	
188	Vema	T. Fault	-40.869	10.723	-43.643	10.847	303.3	South America	North-West Africa		18.9	20.2	24.4
189	Marathon	T. Fault	-44.067	12.617	-44.834	12.658	83.3	South America	North-West Africa		N/A	6.5	6.9
190	Fifteen-Twenty	T. Fault	-44.872	15.199	-46.645	15.349	191.0	South America	North-West Africa	North America	12.7	14.5	
242	MAR 18.5N	T. Fault	-46.610	18.484	-46.415	18.449	20.9	North America	North-West Africa		1.7	1.3	
191	Kane	T. Fault	-44.910	23.617	-46.346	23.847	148.4	North America	North-West Africa		9.1	11.5	12.6
194	Atlantis	T. Fault	-42.700	30.132	-42.020	30.006	67.1	North America	North-West Africa		5.3	5.1	5.2
195	Hayes	T. Fault	-39.038	33.733	-38.248	33.584	75.0	North America	North-West Africa		9.2	10.8	7.9
196	Oceanographer	T. Fault	-36.300	35.295	-34.990	35.047	122.4	North America	North-West Africa		11.8	9.5	12.3
257	MAR 36.9N	T. Fault	-32.956	36.943	-33.191	36.949	20.9	North America	North-West Africa		N/A	3.6	
197	MAR 38N	T. Fault	-31.376	38.043	-30.747	38.013	55.9	North America	North-West Africa		5.6	5.4	
	Charlie Gibbs complex						**315.0**	North America	Eurasia	Porcupine	**26.5**	**34.6**	
198	Charlie Gibbs B	T. Fault	-30.008	52.080	-31.618	52.184	110.5	North America	Porcupine		8.9	NaN	
199	Charlie Gibbs A	T. Fault	-31.671	52.562	-34.691	52.720	204.5	North America	Eurasia	Porcupine	NaN	20.9	
200	Bight	T. Fault	-34.347	56.792	-34.035	56.776	19.1	Greenland	Eurasia	North America	2.2	2.2	
220	Jan Mayen	T. Fault	-12.120	71.702	-8.143	71.182	218.0	Greenland	Eurasia		29.3	N/A	
221	Molloy	T. Fault	3.178	79.018	7.569	78.473	112.8	Greenland	Eurasia		N/A	16.3	
222	Spitsbergen	T. Fault	-1.622	80.352	4.058	79.621	136.5	Greenland	Eurasia		N/A	15.5	
	Southwest Indian Ridge												
150	Bouvet	T. Fault	2.954	-53.693	0.774	-54.912	195.9	Antarctica	Africa		10.6	16.1	29.0
149	Islas Orcadas	T. Fault	6.609	-53.853	5.528	-54.598	108.7	Antarctica	Africa		N/A	10.4	
148	Shaka	T. Fault	9.869	-52.919	8.171	-54.138	176.4	Antarctica	Africa		N/A	22.1	24.7

(*continued on next page*)

Table 2 (*continued*)

			Ridge-transform intersection				Length	Plates			Age offset		
Index	Name	Type[a]	Lon1	Lat1	Lon2	Lat2	km	Plate#1	Plate#2	Plate#3	Age#1	Age#2	R22
147	Du Toit	T. Fault	25.816	-52.575	25.221	-53.506	111.3	Antarctica	Africa		N/A	16.1	16.7
	Andrew Bain complex						**681.9**	Antarctica	Africa		**70.5**	**57.3**	
146	Andrew Bain C	T. Fault	30.511	-49.200	27.839	-52.722	435.3	Antarctica	Africa		N/A	N/A	62.2
144	Andrew Bain A	T. Fault	32.378	-47.145	32.027	-47.997	98.5	Antarctica	Africa		N/A	N/A	12.7
145	Andrew Bain B	T. Fault	31.750	-48.043	30.739	-49.192	148.2	Antarctica	Africa		N/A	N/A	20.8
143	Marion	T. Fault	33.881	-46.086	33.479	-47.111	118.5	Antarctica	Africa		14.5	19	15.5
142	Prince Edward	T. Fault	35.387	-44.746	34.930	-46.068	151.5	Antarctica	Africa		14	22	
141	Eric Simpson	T. Fault	39.347	-43.312	39.187	-44.181	97.5	Antarctica	Africa		11.5	12.5	
	Discovery II complex						**335.4**				**37**	**41**	
140	Discovery II A	T. Fault	41.770	-42.681	41.583	-43.784	123.6	Antarctica	Africa		12.1	16.5	
139	Discovery II B	T. Fault	42.796	-40.886	42.438	-42.772	211.8	Antarctica	Africa		25.4	37.1	
138	Indomed	T. Fault	46.216	-38.935	46.096	-40.018	121.3	Antarctica	Africa		16.4	16.4	
137	Gallieni	T. Fault	52.349	-36.211	52.313	-37.086	97.8	Antarctica	Africa		13.2	15.4	
136	Gazelle	T. Fault	53.435	-35.503	53.416	-36.182	75.6	Antarctica	Africa		9	7.1	
135	Gauss	T. Fault	54.125	-34.795	54.118	-35.270	52.8	Antarctica	Africa		6.1	7	
134	Atlantis II	T. Fault	57.070	-31.883	57.066	-33.648	196.5	Antarctica	Africa		21.1	19.6	27.7
133	Novara	T. Fault	58.383	-31.639	58.381	-31.257	42.5	Antarctica	Africa		6.4	8.1	
132	Melville	T. Fault	60.784	-30.230	60.751	-29.511	80.3	Antarctica	Africa		14.3	13.3	
	South East Indian Ridge												
108	SEIR 71E	T. Fault	70.984	-26.236	71.301	-26.004	40.8	Antarctica	Australia		1.4	1.5	
107	Ter Tholen	T. Fault	77.339	-33.712	78.094	-33.175	92.1	Antarctica	Australia		3.1	3.5	3.1
	Zeewolf complex						**57.0**	Antarctica	Australia		**1.8**	**1.9**	
106	Zeewolf B	T. Fault	78.525	-35.263	78.753	-35.103	27.3	Antarctica	Australia		N/A	N/A	1.0
105	Zeewolf A	T. Fault	78.327	-35.503	78.587	-35.341	29.7	Antarctica	Australia		N/A	N/A	1.0
104	Nieuw Amsterdam	T. Fault	78.253	-37.005	79.145	-36.377	106.0	Antarctica	Australia		4.2	3.8	3.6
103	Hillegom's Hole	T. Fault	78.119	-38.860	78.586	-38.453	61.2	Antarctica	Australia		1.9	3.6	2.0
102	Vlamingh	T. Fault	80.922	-41.079	79.884	-41.803	118.4	Antarctica	Australia		3.8	3.5	4.3
	Geelvinck complex						**293.9**	Antarctica	Australia		**8.6**	**8.4**	
101	Geelvinck B	T. Fault	85.971	-40.968	85.386	-41.459	73.3	Antarctica	Australia		N/A	N/A	2.5
100	Geelvinck A	T. Fault	83.395	-42.878	85.237	-41.438	220.6	Antarctica	Australia		N/A	N/A	
99	SEIR 88E	T. Fault	88.679	-41.708	88.223	-42.116	59.3	Antarctica	Australia		1.7	2	2.1
	SEIR 96E complex						**129.5**	Antarctica	Australia		**3.9**	**3.4**	
98	SEIR 96E A	T. Fault	96.415	-45.347	95.672	-45.983	91.3	Antarctica	Australia		2.8	2.1	2.8
217	SEIR 96E B	T. Fault	96.284	-46.286	96.016	-46.576	38.2	Antarctica	Australia		1.2	1.2	1.3
97	SEIR 100E	T. Fault	100.284	-47.187	99.333	-48.210	134.1	Antarctica	Australia		4.1	3.7	4.1
223	SEIR 102.7E	T. Fault	102.632	-48.018	102.859	-47.753	34.0	Antarctica	Australia		1.1	1.2	1.1
	SEIR 105E complex						**62.0**	Antarctica	Australia		**2.3**	**2.2**	
96	SEIR 105E A	T. Fault	105.018	-48.667	105.222	-48.412	32.2	Antarctica	Australia		1.5	N/A	0.8

(*continued on next page*)

Table 2 (*continued*)

			Ridge-transform intersection				Length	Plates			Age offset		
Index	Name	Type[a]	Lon1	Lat1	Lon2	Lat2	km	Plate#1	Plate#2	Plate#3	Age#1	Age#2	R22
95	SEIR 105E B	T. Fault	105.280	-48.740	105.071	-48.972	29.9	Antarctica	Australia		N/A	0.8	0.6
	SEIR 106E complex						**123.2**	Antarctica	Australia		**3.6**	**3.2**	
94	SEIR 106E A	T. Fault	106.457	-48.843	106.114	-49.296	56.3	Antarctica	Australia		v	1.5	1.7
93	SEIR 106E B	T. Fault	107.040	-48.313	106.643	-48.854	66.9	Antarctica	Australia		1.9	N/A	1.9
92	SEIR 108.5E	T. Fault	108.571	-48.807	108.420	-48.978	22.0	Antarctica	Australia		0.7	0.8	
	Zeehaen complex						**62.6**	Antarctica	Australia		**2.5**	**1.8**	
91	Zeehaen A	T. Fault	114.121	-50.090	113.915	-50.399	37.4	Antarctica	Australia		N/A	0.8	1.1
87	Zeehaen B	T. Fault	114.350	-49.841	114.238	-50.056	25.2	Antarctica	Australia		0.9	N/A	0.9
	Zeehaen complex						**436.6**	Antarctica	Australia		**2.2**	**2**	
86	Heemskerck A	T. Fault	116.030	-49.695	115.870	-49.984	35.1	Antarctica	Australia		0.9	0.9	1.0
90	Heemskerck B	T. Fault	116.378	-49.544	116.525	-49.263	33.1	Antarctica	Australia		1	1.1	1.0
88	Barega	T. Fault	120.538	-49.269	120.155	-50.129	99.5	Antarctica	Australia		2.5	2.8	
85	SEIR 121E	T. Fault	121.013	-48.874	120.817	-49.325	52.1	Antarctica	Australia		1.4	1.5	
84	Nalkari	T. Fault	121.366	-49.708	121.621	-48.996	81.4	Antarctica	Australia		2.4	2.1	
83	SEIR 122.8E	T. Fault	122.901	-49.529	122.679	-49.922	46.4	Antarctica	Australia		1.7	2	
	Warringa complex						**88.9**	Antarctica	Australia		**2.6**	**2.6**	
82	Warringa A	T. Fault	123.320	-49.591	123.524	-49.023	64.9	Antarctica	Australia		1.7	1.8	
81	Warringa B	T. Fault	123.938	-48.860	123.843	-49.067	23.9	Antarctica	Australia		0.9	0.9	
80	Euroka	T. Fault	126.317	-48.682	125.976	-49.742	120.9	Antarctica	Australia		3.9	3.4	3.6
89	Birubi	T. Fault	127.470	-48.826	127.106	-49.978	130.8	Antarctica	Australia		3.9	3.8	
	George V complex						**420.3**	Antarctica	Australia		**13.4**	**9.9**	
216	George V A	T. Fault	139.500	-50.288	139.382	-51.170	98.6	Antarctica	Australia		3.2	N/A	
215	George V B	T. Fault	139.723	-51.122	139.722	-51.802	75.5	Antarctica	Australia		2.1	N/A	
214	George V C	T. Fault	140.614	-54.092	140.470	-51.879	246.2	Antarctica	Australia		5.5	N/A	
213	St Vincent	T. Fault	144.130	-54.225	144.119	-54.839	68.2	Antarctica	Australia		2.2	1.7	
	Tasman complex						**339.3**	Antarctica	Australia		**20.5**	**25.6**	
212	Tasman A	T. Fault	146.572	-55.780	146.417	-54.768	113.0	Antarctica	Australia		4	N/A	
211	Tasman B	T. Fault	147.953	-57.561	147.402	-55.824	196.0	Antarctica	Australia		N/A	N/A	
210	Tasman C	T. Fault	148.477	-57.781	148.361	-57.517	30.2	Antarctica	Australia		1.1	N/A	
78	Tasman D	T. Fault	148.852	-57.736	149.723	-59.640	217.6	Antarctica	Australia		N/A	4	
77	Tasman E	T. Fault	150.401	-59.511	150.937	-60.491	112.9	Antarctica	Australia		N/A	4.1	
79	Balleny	T. Fault	153.524	-59.995	156.170	-62.935	356.1	Antarctica	Australia	Marie Byrd Land	8.8	N/A	
	Pacific Antarctic Ridge												
76	PAR 161E	T. Fault	161.023	-61.496	161.773	-62.063	74.4	Marie Byrd Land	Pacific		N/A	2.5	
208	Hjort	T. Fault	162.798	-61.739	163.833	-62.452	95.8	Marie Byrd Land	Pacific		N/A	N/A	
209	PAR 165E	T. Fault	165.036	-62.041	166.506	-63.025	132.8	Marie Byrd Land	Pacific		N/A	N/A	
249	PAR 168E	T. Fault	168.162	-62.860	167.648	-62.562	42.2	Marie Byrd Land	Pacific		N/A	N/A	
248	PAR 171E	T. Fault	173.449	-64.801	169.620	-62.277	340.6	Marie Byrd Land	Pacific		N/A	N/A	
75	PAR 175E	T. Fault	175.144	-64.362	174.952	-64.254	15.2	Marie Byrd Land	Pacific		N/A	N/A	

(*continued on next page*)

Table 2 (*continued*)

			Ridge-transform intersection				Length	Plates			Age offset		
Index	Name	Type[a]	Lon1	Lat1	Lon2	Lat2	km	Plate#1	Plate#2	Plate#3	Age#1	Age#2	R22
	Emerald complex						**354.2**	Marie Byrd Land	Pacific		**N/A**	**N/A**	
247	Emerald A	T. Fault	176.350	-64.703	175.588	-64.210	65.8	Marie Byrd Land	Pacific		N/A	N/A	
246	Emerald B	T. Fault	177.607	-65.010	176.722	-64.420	78.1	Marie Byrd Land	Pacific		N/A	N/A	
245	Emerald C	T. Fault	178.510	-65.299	177.970	-64.852	55.7	Marie Byrd Land	Pacific		N/A	N/A	
244	Terror	T. Fault	181.201	-66.176	179.284	-65.033	154.6	Marie Byrd Land	Pacific		N/A	8.9	
74	Erebus	T. Fault	-176.030	-65.285	-175.414	-65.619	46.8	Marie Byrd Land	Pacific		2.3	2.9	
45	Pitman	T. Fault	-171.204	-64.327	-170.468	-64.684	53.1	Marie Byrd Land	Pacific		3.6	3.2	2.3
47	Heirtzler	T. Fault	-164.115	-63.010	-163.539	-63.219	37.1	Marie Byrd Land	Pacific		1.9	1.7	
73	La Rose	T. Fault	-161.835	-62.463	-160.595	-63.131	97.4	Marie Byrd Land	Pacific		3.6	3.5	
258	PAR 159W	T. Fault	-159.035	-63.099	-159.909	-62.678	64.4	Marie Byrd Land	Pacific		N/A	N/A	
44	Le Renard	T. Fault	-158.362	-62.648	-157.306	-63.159	78.2	Marie Byrd Land	Pacific		4.2	3.7	
43	Saint Exupery	T. Fault	-155.751	-62.146	-155.087	-62.353	41.3	Marie Byrd Land	Pacific		1.2	1.8	
42	L'Astronome	T. Fault	-151.286	-59.478	-150.351	-59.750	60.8	Marie Byrd Land	Pacific		2	1.9	
41	Le Geographe	T. Fault	-147.944	-57.482	-146.970	-57.779	66.8	Marie Byrd Land	Pacific		2.1	2.1	
48	Udintsev	T. Fault	-144.636	-55.708	-140.085	-57.112	323.7	Marie Byrd Land	Pacific		10.3	12.4	
40	Herron	T. Fault	-139.191	-56.236	-138.871	-56.331	22.5	Marie Byrd Land	Pacific		N/A	0.8	0.7
39	Hollister	T. Fault	-136.962	-54.141	-135.302	-54.638	121.3	Marie Byrd Land	Pacific		3.2	3.3	3.4
38	Tharp	T. Fault	-127.891	-55.389	-134.408	-53.787	456.5	Marie Byrd Land	Pacific		15.3	20.8	11.9
37	Heezen	T. Fault	-127.389	-54.872	-121.826	-56.012	373.1	Marie Byrd Land	Pacific		7.2	10.1	9.7
	Raitt complex						**143.3**	Marie Byrd Land	Pacific		**3.3**	**3.7**	
34	Raitt A	T. Fault	-120.701	-54.213	-119.489	-54.477	84.0	Marie Byrd Land	Pacific		N/A	N/A	2.0
35	Raitt B	T. Fault	-119.406	-54.386	-118.538	-54.557	59.3	Marie Byrd Land	Pacific		N/A	N/A	1.4
33	Vacquier	T. Fault	-118.372	-52.981	-117.684	-53.088	47.8	Marie Byrd Land	Pacific		1.5	1.4	0.6
36	Menard	T. Fault	-113.887	-49.835	-116.577	-49.350	201.5	Marie Byrd Land	Pacific		5.3	5.7	
	East Pacific Rise												
5	Southeastern Juan Fernandez Transfer Zone	T. Zone	-112.002	-34.761	-110.811	-35.101	118.8	Marie Byrd Land	Pacific	Juan Fernandez Microplate	N/A	N/A	
6	Southwestern Juan Fernandez Transfer Zone	T. Zone	-110.811	-35.101	-109.266	-34.611	152.9	Marie Byrd Land	Pacific	Juan Fernandez Microplate	N/A	N/A	
4	Northern Juan Fernandez Transfer Zone	T. Zone	-109.791	-32.115	-112.020	-31.723	217.1	Nazca	Pacific	Juan Fernandez Microplate	N/A	N/A	
3	Southern Easter Transform Zone	T. Zone	-114.793	-26.834	-112.953	-26.799	182.6	Nazca	Pacific	Easter Island Microplate	N/A	N/A	
8	Easter Microplate A Transfer Zone	T. Zone	-116.265	-24.565	-115.907	-24.401	40.6	Pacific	Easter Island Microplate		N/A	N/A	
9	Easter Microplate B Transfer Zone	T. Zone	-115.939	-24.298	-115.325	-24.042	68.4	Pacific	Easter Island Microplate		N/A	N/A	
7	Easter Microplate North Transfer Zone	T. Zone	-115.552	-23.491	-115.042	-23.406	52.9	Pacific	Easter Island Microplate		N/A	N/A	
2	Northern Pito Transform Zone	T. Zone	-112.304	-22.785	-114.525	-23.047	235.4	Pacific	Easter Island Microplate	Pacific	N/A	N/A	
61	Pito W	T. Fault	-114.860	-23.049	-114.536	-23.053	33.2	Pacific	Easter Island Microplate	Nazca	0.4	N/A	
	Garrett complex						**117.7**	Pacific	Nazca		**N/A**	**1.7**	
228	Garrett A	T. Fault	-112.300	-13.374	-111.903	-13.478	44.6	Pacific	Nazca		N/A	N/A	

(*continued on next page*)

Table 2 (*continued*)

			Ridge-transform intersection				Length	Plates			Age offset		
Index	Name	Type[a]	Lon1	Lat1	Lon2	Lat2	km	Plate#1	Plate#2	Plate#3	Age#1	Age#2	R22
229	Garrett B	T. Fault	-111.858	-13.425	-111.715	-13.459	16.0	Pacific	Nazca		N/A	N/A	
230	Garrett C	T. Fault	-111.677	-13.411	-111.377	-13.491	33.7	Pacific	Nazca		N/A	N/A	
231	Garrett D	T. Fault	-111.358	-13.447	-111.152	-13.509	23.4	Pacific	Nazca		N/A	N/A	
	Wilkes complex						**93.4**	Pacific	Nazca		**N/A**	**2.4**	
62	Wilkes A	T. Fault	-109.214	-9.016	-109.349	-8.985	15.2	Pacific	Nazca		N/A	N/A	
71	Wilkes B	T. Fault	-109.153	-8.947	-108.473	-9.153	78.2	Pacific	Nazca		N/A	N/A	
10	Wilkes nanoplate transfer zone	T. Zone	-108.512	-8.617	-108.102	-8.770	48.2	Pacific	Nazca	Wilkes Nanoplate	N/A	N/A	
70	Yaquina	T. Fault	-107.408	-6.209	-107.199	-6.260	23.8	Pacific	Nazca		0.4	N/A	
	Gofar complex						**157.3**	Pacific	Nazca		**N/A**	**N/A**	
29	Gofar A	T. Fault	-106.202	-4.510	-105.443	-4.689	86.5	Pacific	Nazca		N/A	2.4	
67	Gofar B	T. Fault	-105.175	-4.601	-105.399	-4.553	25.4	Pacific	Nazca		N/A	N/A	
49	Gofar C	T. Fault	-105.106	-4.513	-104.705	-4.594	45.4	Pacific	Nazca		N/A	N/A	
	Discovery complex						**62.8**	Pacific	Nazca		**N/A**	**N/A**	
50	Discovery B	T. Fault	-103.900	-4.032	-104.135	-3.986	26.6	Pacific	Nazca		N/A	N/A	
51	Discovery A	T. Fault	-104.518	-3.990	-104.195	-4.026	36.1	Pacific	Nazca		N/A	N/A	
	Quebrada complex						**98.7**	Pacific	Nazca		**N/A**	**1.6**	
52	Quebrada A	T. Fault	-103.711	-3.737	-103.585	-3.768	14.3	Pacific	Nazca		N/A	N/A	
53	Quebrada B	T. Fault	-103.520	-3.719	-103.341	-3.750	20.1	Pacific	Nazca		N/A	N/A	
54	Quebrada C	T. Fault	-103.281	-3.680	-103.050	-3.732	26.3	Pacific	Nazca		N/A	N/A	
55	Quebrada D	T. Fault	-103.023	-3.699	-102.689	-3.769	37.9	Pacific	Nazca		N/A	N/A	
	Siqueiros complex						**121.0**	Pacific	Cocos		3.5	3.4	
233	Siqueiros D	T. Fault	-103.307	8.338	-102.944	8.432	41.5	Pacific	Cocos		N/A	N/A	
232	Siqueiros C	T. Fault	-103.556	8.321	-103.341	8.388	24.7	Pacific	Cocos		N/A	N/A	
57	Siqueiros B	T. Fault	-103.885	8.338	-103.575	8.392	34.6	Pacific	Cocos		N/A	N/A	
26	Siqueiros A	T. Fault	-104.157	8.374	-103.977	8.406	20.1	Pacific	Cocos		N/A	N/A	
12	Clipperton	T. Fault	-104.315	10.183	-103.607	10.285	78.3	Pacific	Cocos		1.6	1.6	
56	Orozco	T. Fault	-105.294	15.359	-104.902	15.431	42.9	Pacific	Cocos		N/A	0.7	
	Riviera complex						**366.8**	Pacific	Riviera		7.8	9.1	
13	Riviera C	T. Fault	-106.266	18.512	-108.151	19.079	209.2	Pacific	Riviera	Cocos	N/A	N/A	
69	Riviera B	T. Fault	-108.877	19.575	-108.164	19.221	84.6	Pacific	Riviera		N/A	N/A	
68	Riviera A	T. Fault	-108.880	19.656	-109.457	20.023	73.1	Pacific	Riviera		N/A	N/A	
24	Tomayo	T. Fault	-108.069	22.923	-108.616	23.234	65.8	Riviera	Mexico		N/A	N/A	
14	South Pescadero	T. Fault	-108.387	23.631	-108.874	23.962	62.0	Mexico	Baja California		N/A	N/A	
15	Central Pescadero	T. Fault	-108.848	24.035	-109.237	24.365	54.3	Mexico	Baja California		N/A	N/A	
25	Atl	T. Fault	-109.934	25.349	-109.093	24.644	116.4	Mexico	Baja California		N/A	N/A	
65	Farallon	T. Fault	-110.771	26.322	-109.774	25.573	131.5	Mexico	Baja California		N/A	N/A	
66	Carmen	T. Fault	-111.440	26.950	-110.710	26.420	93.5	Mexico	Baja California		N/A	N/A	
234	Guaymas	T. Fault	-111.336	27.519	-113.265	28.882	244.1	Mexico	Baja California		N/A	N/A	
235	Del Mar	T. Fault	-113.211	29.008	-113.927	29.570	93.4	Mexico	Baja California		N/A	N/A	
	Gorda & Juan de Fuca Ridges												

(*continued on next page*)

Table 2 (*continued*)

			Ridge-transform intersection				Length	Plates			Age offset		
Index	Name	Type[a]	Lon1	Lat1	Lon2	Lat2	km	Plate#1	Plate#2	Plate#3	Age#1	Age#2	R22
46	Mendocino	T. Fault	-127.446	40.377	-124.820	40.377	222.4	Pacific	Vancouver				
	Blanco complex						**461.9**	**Pacific**	**Vancouver**				
58	Blanco A	T. Fault	-130.434	44.496	-129.673	44.252	66.4						2.6
59	Blanco C	T. Fault	-129.081	43.946	-128.687	43.853	33.2						1.4
60	Blanco D	T. Fault	-128.688	43.696	-127.582	43.371	96.2						5.8
63	Blanco E	T. Fault	-126.597	43.001	-127.513	43.255	79.8						1.8
64	Blanco B	T. Fault	-129.078	43.996	-129.610	44.167	46.6						2.0
1	Sovanco	T. Zone	-128.773	48.825	-130.631	49.074	139.7						
	Andaman Sea												
182	Andaman	T. Fault	95.187	11.108	95.167	12.704	177.4	Andaman Sea West	Andaman Sea East		3.8	5.8	
	Bismark Sea												
260	Willaumez	T. Fault	148.929	-3.417	147.818	-2.871	137.5	North Bismark Basin	South Bismark Basin		N/A	N/A	
256	Djaul	T. Fault	151.431	-3.733	150.513	-3.052	127.0	North Bismark Basin	South Bismark Basin		N/A	N/A	
261	Weitin	T. Fault	152.639	-4.207	152.193	-3.725	73.0	North Bismark Basin	South Bismark Basin		N/A	N/A	
	Fidji Basin												
259	North Fidji A	T. Fault	177.419	-16.294	178.104	-16.141	75.9	North Fidji Basin	Fidji		N/A	N/A	
243	North Fidji B	T. Fault	176.181	-16.573	177.380	-16.550	127.9	North Fidji Basin	Fidji		N/A	N/A	
	Woodlark Basin												
192	Moresby	T. Fault	154.210	-10.293	154.234	-9.932	40.2	Woodlark Basin			N/A	N/A	
193	Woodlark 156E	T. Fault	156.105	-9.546	156.085	-9.424	13.8	Woodlark Basin			N/A	N/A	
	Lau Basin												
224	Lau Extensional Transform Zone	T. Fault	-179.088	-15.171	-176.641	-17.024	333.5	Lau-Colville Ridge			N/A	N/A	
262	Futuna	T. Fault	-178.707	-14.194	-177.393	-14.413	145.0	Lau-Colville Ridge			N/A	N/A	

[a] T. Fault: Transform Fault; T. Zone: Trasform Zone.

faults). Spreading obliquity may also control the length of both segments and lateral offsets; at highly oblique ridge sections, NTOs may have lateral offsets that are larger than the rift valley width (Fig. 3b), while along ridge sections with low obliquity, the lateral offset of NTOs may be shorter than the ridge valley width (<10-20 km), as seen along the Reykjanes Ridge [Panasiuk et al., 2025]. In these cases, adjacent ridge segments lay within a continuous rift valley with ill-defined segmentation. Off-axis bathymetry can reveal the wakes of NTO traces [Harper et al., 2023] that may be exploited to identify NTOs at the ridge axis [e.g., Tucholke et al., 1997]. In contrast, fast-spreading ridges often exhibit overlapping segments. The zone within the non-transform area (gray zone in Fig. 2b, c), corresponds then to lithosphere accreted along the ridge axis, and subsequently modified by tectonic, volcanic, and hydrothermal processes occurring and interacting at NTOs [e.g., Sempéré and Macdonald, 1986]. Based on the MAPRIDGES ridge segmentation, we identify1058 NTOs, with less than 20% of them poorly mapped or unmapped.

For the subaerial portion of the Mid-Atlantic Ridge along Iceland, we have not mapped NTOs owing to a ridge geometry structure showing numerous overlapping segments and which differs fundamentally from that of submerged ridge segments. The geometries of NTOs and associated parameters are thus based on the detailed digitization of ridge segments and on the calculated spreading direction, excluding Iceland.

Spreading rate is a parameter that influences ridge segmentation and therefore our database includes spreading rates and direction for each ridge segment. To assign these parameters, and to calculate along- and across-axis (lateral) offsets for both underlapping and overlapping NTOs, we use the two most widely adopted present-day plate kinematic models available: the MORVEL (averaged plate motion for the last ~3 Myr, DeMets et al. [2010]), and the GSRM model (geodetically based plate motion, Kreemer et al. [2014]), discussed in detail in the following section. These models are complemented with published or derived poles (e.g., specific back-arc ridge sections that are not included in the global models [Seno et al., 1993; Nishimura et al., 2004; Sleeper and Martinez, 2016]). The present-day poles of rotation and angular velocities for 39 pairs of plates (Supplementary Materials Table S2) are used to assign spreading rate and direction based on the different plate boundary sections (e.g., Fig. 1 in DeMets et al. [2010]).

3. Quantification of the global mid-ocean ridge system

The MAPRIDGES database is used to estimate the total length of the global mid-ocean ridge and back-arc basin system (Table 3), which include ridge segments and their transform and non-transform offsets. We calculate a total global transform fault length of ~27000 km (262 features) and of 1300 km associated with transform zones (10 features). Only 10 transform faults are identified in back-arc basins, with a cumulative length of ~1200 km. Bird [2003] and more recently Hasterok

Table 3
Summary of ridge length, offsets of NTOs (along-and across axis), and transform fault and zone lengths calculated from the MAPRIDGES dataset. NTO offsets are calculated using the two plate rotation models based on the MORVEL and GSRM models (see Supplementary Materials Table S1 and text for details).

	Global		MORs		Back-Arcs	
A) Ridge segments						
Number of segments	1471		1268		203	
% of well-mapped segments	89		88		97	
Cumulative length (RL), all segments, km	71206		61763		9443	
Cumulative ength (RL), well mapped segments, km	60270		51349		8921	
% of well mapped ridge length	84.6		83.1		94.5	
Average segment length (standard deviation), km [1]	46.0 (43.2)		46.1 (44.6)		45.5 (34.3)	
B) Transforms						
Transform faults, #	262		252		10	
Transform zones, #	10		10		0	
Transform faults, km	27000		25749		1251	
Transform zones, km	1257		1257		0	
Total transform faults and zones	28257		27006		1251	
C) Non-transform offsets						
Model	*MORVEL*	*GSRM*	*MORVEL*	*GSRM*	*MORVEL*	*GSRM*
Along axis offset, AO [2]						
AO of NTOs Overerlap, km	-4997	-4993	-3941	-3941	-753	-754
AO of NTOs Underlap, km	1732	1683	1412	1367	374	372
AO, all NTOs	6729	6676	5353	5308	1127	1126
Lateral offset, LO [2]						
LO of underlapping NTOs, km	5338	5334	3418	3521	171	188
LO of overlapping NTOs, km	3881	3984	4859	5178	325	364
LO, all NTOs	9219	9318	8277	8699	496	552
% w.r.t. transform offsets	33	33	31	32	40	44
D) "EFFECTIVE" RIDGE LENGTH*	67941	67896	59234	59189	9064	9061
E) TOTAL LATERAL OFFSETS	37476	37575	35283	35705	1747	1803
F) TOTAL RIDGE PLATE BOUNDARY	105417	105471	94517	94894	10811	10864

[1]: Calculated from well mapped ridge segments only.
*Total ridge length includes the subaerial section of the Mid-Atlantic Ridge in Iceland, with a cumulative length of 880 km associated with numerous overlapping segments.
**Corrected ridge length corresponds to the cumulative ridge length, and adding the underlap length and substracting the overlap length of NTOs.
[2] From the 1058 discontinuities, 13 do not have an attributed pole of rotation, nor inferred spreading direction and rate, and hence have no AO nor LO value attributed.

et al. [2022] report lengths of transform plate boundaries of ~48000 km or ~100000 km, respectively, encompassing both transform faults and transform zones along mid-ocean ridges, as well as major strike-slip plate boundaries or fracture zones away from ridges. Hence, the lengths including transform boundaries reported by previous studies and listed in Table 1 are not always directly comparable to the cumulative transform length that we calculate here and report in Table 3 due to differences in data and methodology.

Mid-ocean ridge segments are also shifted laterally at NTOs (Figs. 2, 3a, b). The role of NTOs in estimating the geometry and total length of divergent plate boundaries has not been studied in prior publications. MAPRIDGES provides the first report of NTO lateral offsets (LO and LO_{mean} in Fig. 2 for underlapping and overlapping NTOs respectively). These parameters are calculated in a direction parallel to that of spreading, which was computed from the modified MORVEL and GSRM rotation plate models (see above and Supplementary Materials Table S2). Table 3 thus reports NTO offset lengths for both the MORVEL and GMSR models, and shows that differences between these two models are negligible (e.g., cumulative lateral offset of NTOs of ~9200 and. 9300 km respectively, see Table 3); from hereon we report in the text only the values from the MORVEL model for simplicity. The calculated cumulative lateral offset from our database is ~8800 km (Table 3), nearly a third of the cumulative length of transform faults and zones along ridges. Mid-ocean ridges account for the bulk of this cumulated lateral ridge offset (~8300 km), with only ~6% associated with back-arc spreading centres (~500 km).

The MAPRIDGE database includes 1471 ridge segments along mid-ocean ridges and back-arc spreading centres, with an estimated cumulative length of ~71200 km. Excluding back-arc basins, mid-ocean ridges exhibit a cumulative length of ~61800 km (1258 segments), with ~51300 km (~83%) of ridge segments mapped based on multibeam bathymetry. Part of this mid-ocean ridge system is the subaerial portion of the Mid-Atlantic Ridge along Iceland (ICE in Fig. 1), which extends ~880 km and displays significant overlaps and along-axis gaps between groups of segments. The cumulative length of back-arc systems is ~9400 km (213 segments), with ~8900 km of well-mapped segments (~95%).

These cumulative ridge lengths reported above do not consider the along-axis overlap and underlap segments at NTOs (AO in Fig. 2), that amount ~4800 and 1800 km respectively (Table 3). As we assume that transform faults and zones follow meridians of the pole of rotation, their along-axis offset AO is zero. The NTO overlap and underlap, calculated in the direction perpendicular to spreading, can be respectively subtracted from and added to obtain a corrected ridge length. Therefore, we estimate that the global "effective" ridge length is ~67900 km globally, with ~59.000 km corresponding to mid-ocean ridges and ~9000 km to back-arc spreading centres. Because the differences in lengths calculated with the two plate models MORVEL and GSRM are negligible, we suggest thatfor the global analysis presented here the errors in plate motion models are also negligible and without significant impact.

Finally, with this database we can estimate the total length of divergent plate boundaries, by including the "effective" ridge length, the lateral offsets of NTOs, transform faults, and transform zones. This corresponds to ~105400 km, with ~94500 km corresponding to mid-ocean ridge plate boundaries and ~10800 km to those linked to back-arc spreading centres (Table 3).

MAPRIDGES provides a digital plate boundary geometry and location that is morea accurate and therefore improved from that of other

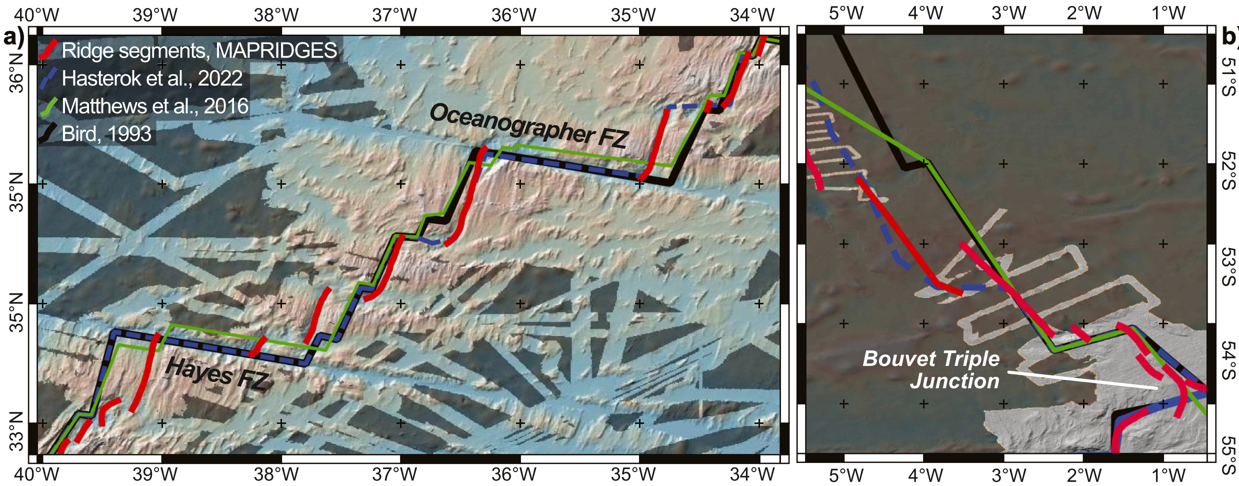

Fig. 4. Comparison of selected published ridge geometries [Bird, 2003; Matthews et al., 2016; Hasterok et al., 2022] and that of MAPRIDGES at the Northern Mid-Atlantic Ridge (a), an area well covered by bathymetry data, and (b) the Southern Mid-Atlantic Ridge North of the Bouvet Triple Junction, showing ridge sections and off-axis areas with limited or no multibeam data coverage.

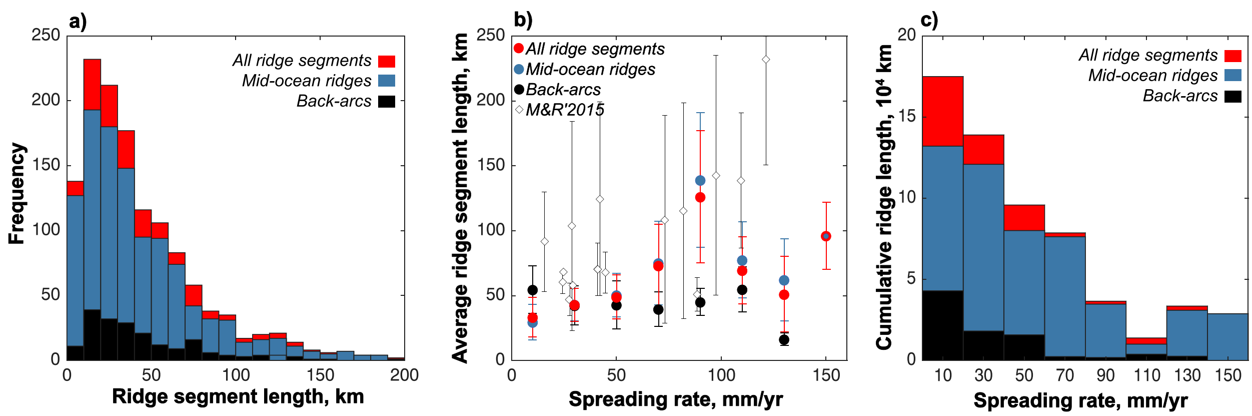

Fig. 5. Ridge segment length of mid-ocean ridges, back-arc spreading centres and the global ridge system: a) Frequency distribution of ridge segment length; b) Average ridge segment length vs. spreading rate. Error bars correspond to the standard deviation. M&R'2015 corresponds to averages (error bars are one-sigma standard deviations) for a set of globally distributed sites reported by Murton and Rona [2015]; c) Cumulative ridge length as a function of spreading rate. In this figure we report values calculated from well-mapped ridge segments.

published models. Fig. 4 illustrates the location of this plate boundary at selected sites according to various models, showing differences that exceed 10 km at many sites, and reaching several tens of km along certain ridge segments or discontinuities. The detailed definition of MAPRIDGES ridge axis geometry will improve studies linking ridge segmentation to axial processes (e.g., seismicity, geochemistry, tectonics, volcanism, hydrothermal activity, etc.) and budgets associated with their modelling (e.g., chemical fluxes, magmatic and volcanic production).

4. Analysis of the global mid-ocean ridge system based on MAPRIDGES database

The segmentation of global mid-ocean ridge system (Fig. 5) may be related to magmatic processes and melt supply to the axis from the mantle, and to the general history and dynamics of oceanic spreading, like the along-axis offset propagation [e.g., Whitehead et al., 1984; Harper et al., 2023], or the overall obliquity of the ridge relative to spreading [e.g., Abelson and Anon, 1997; Patriat et al., 1997; Murton and Parson, 1993; Fournier et al., 2004], among other processes [Carbotte et al., 2015]. For both transforms and non-transform offsets, their length may be linked to the thermal structure, mantle upwelling and melt production, rheology of the lithosphere, shear strength, and the coupling across these boundaries [e.g., Oldenburg and Brune, 1975; Whitehead et al., 1984; Schouten et al., 1985; Sandwell, 1986; Grindlay and Fox, 1993; Dauteuil et al., 2002; Sibrant et al., 2021; Chen et al., 2023]. These parameters and processes may impact the deformation within the mid-ocean ridge system and its seismic behaviour, fluid circulation, etc [e.g., Roland et al., 2010; Wolfson-Schwehr and Boettcher, 2019; Ren et al., 2022; Schierjott et al., 2023].

Non-transform discontinuities bounding segments display both along- and lateral (across-axis) offsets (Fig. 2, AO and LO, respectively). These NTOs correspond to a wide variety of features, including overlapping-spreading centres mainly occurring at fast-spreading centres and tectonically dominated discontinuities at slow-spreading ridges, that may exhibit both overlap and underlap (e.g., Fig. 3). These discontinuities and the ridge segments that they bound have been categorized hierarchically [e.g., Macdonald et al., 1991], with a broad correlation with the lateral offset length that may be linked to the underlying mantle and lithospheric processes, which vary among ridges with varying spreading rate [Carbotte et al., 2015]. MAPRIDGES provides a global view on the geometry of these offsets, and their variation with spreading rate that may contribute to a better understanding of their nature. In particular, MAPRIDGES may facilitate quantitative analyses of observables (seismicity, geochemistry, bathymetry, distribution of hydrothermal activity, etc.), possible proxies for parameters such as mantle temperature, composition, or melt supply at the ridge axis impacting ridge structure and segmentation.

4.1. Length of segments

Taking into account solely well-mapped ridge segments, we observe that the length of mid-ocean ridge segments in large oceans vary with spreading rate, whereas the length of individual ridge segments in back-arc basins is less variable (Fig. 5). However, the average ridge segment length is ~46 km globally, for both back-arc and mid-ocean ridge segments. Note that our dataset also includes numerous short segments (less than 30 km), and a few segments with lengths greater than 100 km (Fig. 5b). This segment length distribution is broadly consistent with the ranges reported in earlier studies (typically 40-100 km [e.g., Schouten et al., 1985; Macdonald et al., 1991; Sempéré et al., 1990b; Carbotte et al., 2015]). Prior studies proposed an increase in ridge segment length with increasing spreading rate [e.g., Schouten et al., 1985; Murton and Rona, 2015]. While the Murton and Rona [2015] study covered a significant portion of the global ridge system (540 segments), their study was based on free-air gravity data instead of multibeam bathymetry, and encompassing both mid-ocean ridges and back-arcs in their compilation. The MAPRIDGES database shows that back-arcs ridge segments exhibit average lengths varying between ~20 and 60 km, but do not show a clear variation with spreading rate. Average mid-ocean ridge segment lengths show however an overall increase with higher spreading rates (Fig. 5b), that to a first order is consistent with that reported by Murton and Rona [2015]. In contrast, the cumulative length of mid-ocean ridges decreases as the extension rate increases (Fig. 5c). Above 80-100 mm/yr this trend breaks down, and the data lacks a clear dependence on spreading rate (Fig. 5b, c). At all spreading rates we observe significant variability in segment lengths, which is consistent with observations reported at different mid-ocean ridge sections (e.g., 20-80 km for the northern Mid-Atlantic Ridge [Schouten et al., 1985; Shaw, 1992]).

4.2. Along-axis offsets (AL) of non-transform discontinuities

Non-transform offsets show average along-axis overlaps and underlaps of ~7.5 and 4.5 km respectively (Fig. 6a, b), that correspond to 10-15% of the average ridge segment length. At spreading velocities below 80 mm/yr, our database documents a gradual decrease in the underlap from ~6 to ~3 km with decreasing spreading rate (Fig. 6b). At velocities

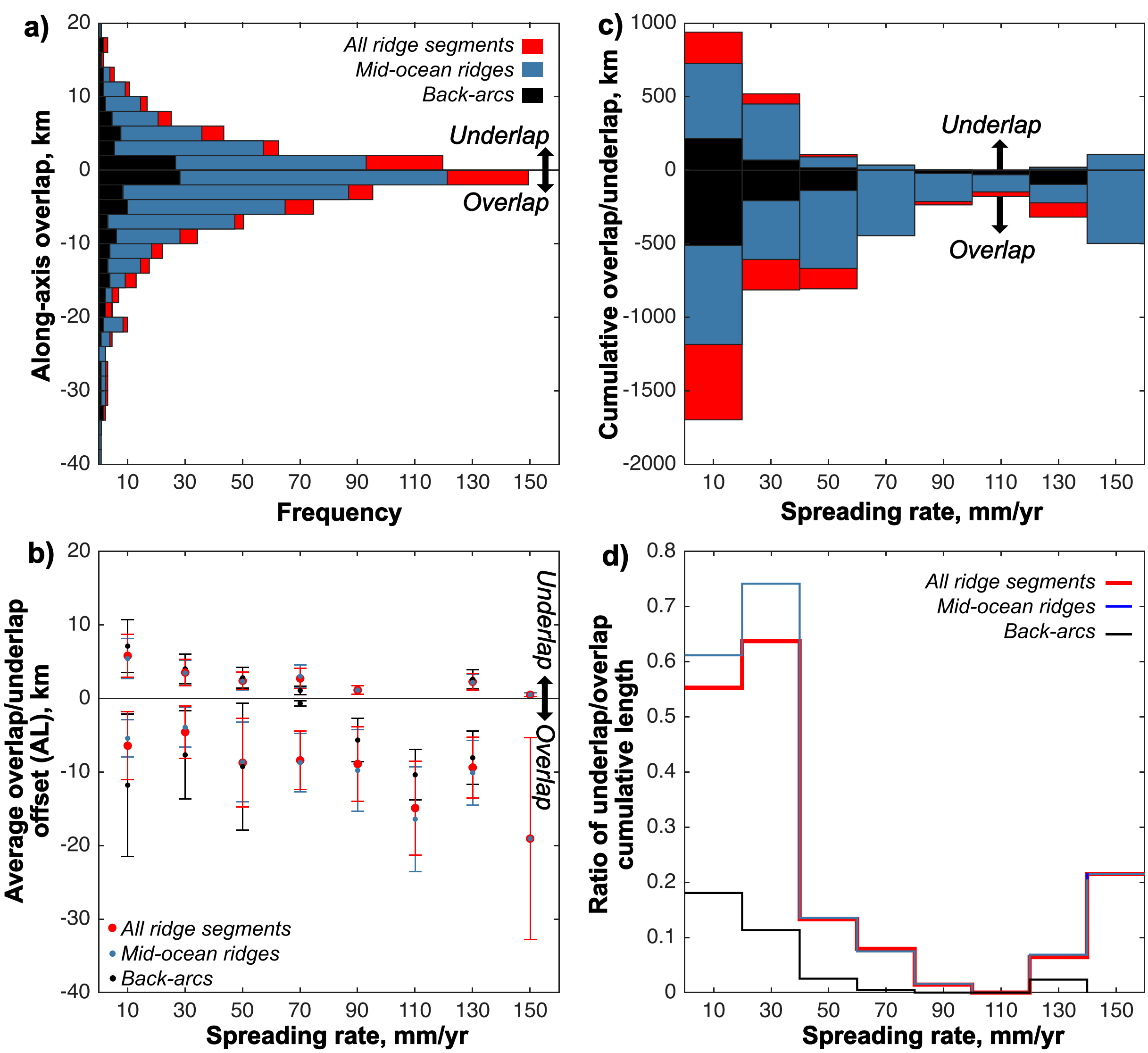

Fig. 6. Along-axis offset of NTOs: a) Frequency of both overlap and underlap along-axis; b) Average along-axis offset for both underlapping and overlapping non-transform offset s vs. spreading rate. Error bars are equal to a standard deviation; c) Cumulative along axis overlap and underlap vs. spreading rate. d) Ratio between the cumulative length of underlaps and overlap vs. spreading rate.

greater than 80-100 mm/yr, the underlap varies at lengths below 4 km with no correlation with spreading rate. Overlap length is in general larger than overlap at all spreading rates, and overlaps display no clear correlation with spreading rate, while underlap length decreases at rates below 80-100 mm/yr (Fig. 6b). The cumulative length for both underlapping and overlapping offsets shows a similar pattern to that of cumulative ridge segment length (Fig. 6c), with a gradual decrease at spreading rates at velocities less than 80-100 mm/yr, and no clear pattern at higher rates both along mid-ocean ridges and back-arc spreading centres. In general overlaps account for a larger proportion of NTOs, as shown by ratios between underlap and overlap lengths below 1 (Fig. 6d). With increasing spreading rate, this ratio decreases from ~0.6-0.7 to less than 0.1 at spreading rates below 80-120 mm/yr, followed by an increase to 0.2 at higher rates.

4.3. Lateral offsets (LO) of non-transform discontinuities and transform faults

Lateral offsets at ridge discontinuities, and the associated age offset, are widely regarded as first-order parameters linked to their mode of deformation. The formation of transform faults and their long-term stability, as opposed to non-transform offsets (NTOs), is linked to a mechanical threshold involving lithospheric thickness and thermal structure (controlled by the offset geometry) among other parameters [e.g., Naar and Hey, 1989; Harper et al., 2023; Sibrant et al., 2021]. In this framework, transform faults are expected to represent stable plate boundaries characterized by localized deformation, whereas NTOs reflect more distributed and potentially transient strain accommodation.

Our systematic mapping of ridge discontinuities allows a characterization and comparison of both transform and non-transform offsets (Fig. 7). While transform faults are associated with larger mean lateral (~103 km) and age (~3.4 Myr) offsets, NTOs have smaller offset and age values (mean ~9 km and ~0.45 Myr), although the distributions of these parameters show significant overlap (Figs. 2, 7). There is also a general inverse power law relationship between lateral offsets of transform faults and NTOs and their frequency (Fig. 7a, c), that breaks down at very short offsets (e.g., spatial resolution of data, lithospheric controls). Most transform faults cluster at lateral offsets less than 100 km and age offsets less than 10 Myr (Fig. 7a, b), whereas the majority of NTOs fall below 20 km and 1 Myr, respectively (Fig. 7c, d). However, there are numerous transform faults with length values that overlap with those of NTOs (less than 20 km, Fig. 7c), mainly along oblique ridge

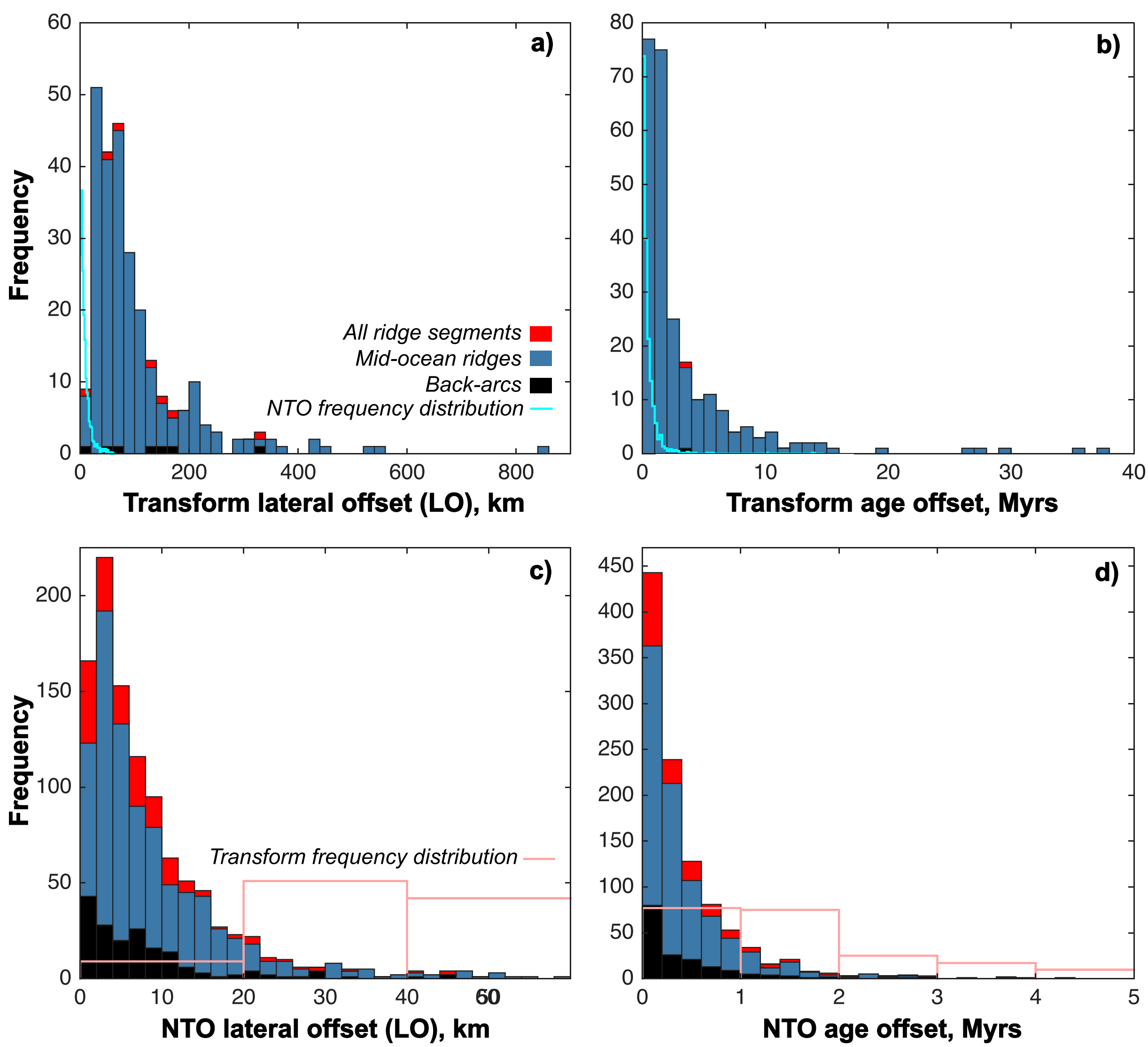

Fig. 7. a) Frequency distribution of lateral offset of transform faults and zones and b) corresponding age offset calculated from spreading rate and measured lateral offset. c)Frequency distribution of NTOs lateral offsets and d) corresponding age offsets. The frequency distribution of transforms is also show in c) and D, and that of NTOs (divided by a factor of 6 to facilitate visualization) in a) and b), to show the overlap in their offsets.

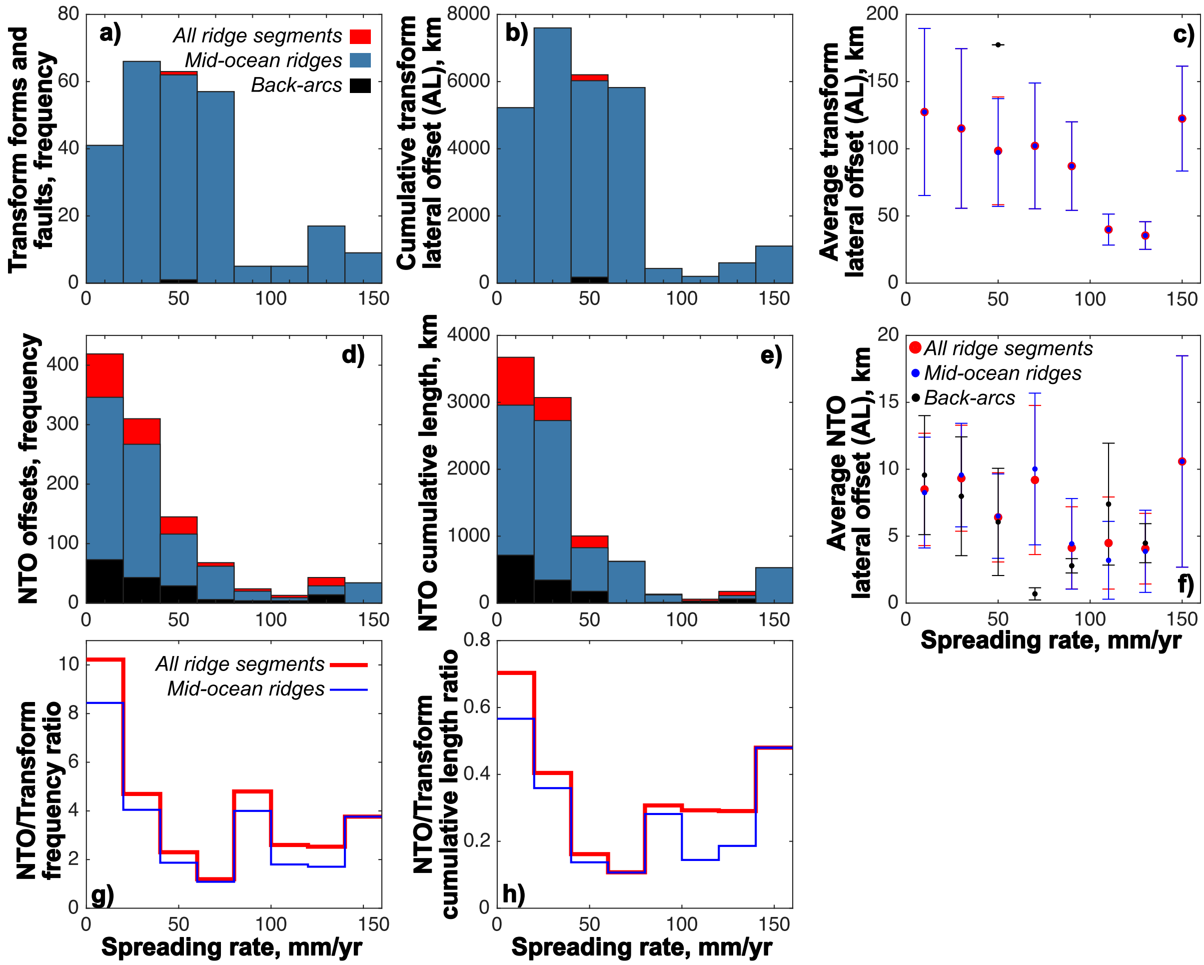

Fig. 8. Transform faults and zones: spreading rate vs. a) frequency, b) cumulative lateral offset, and c) average transform length. Non-transform offsets: spreading rate vs. d) frequency, e) cumulative length, and f) average lateral offset length. Figure g) reports the ratio the ratio of NTO frequency over that of transforms vs. spreading rate, and h) the ratio of cumulative length vs. spreading rate.

sections (e.g., Gulf of Aden), or short intra-transform segments (e.g., Wilkes or Garrett transform fault systems). These global patterns primarily correspond to those of mid-ocean ridges, as transform faults are scarce along back-arc systems. Finally, transform faults concentrate along ridges spreading at <100 mm/yr (Fig. 8a, b), and show an overall decrease in length with increasing spreading rate from ~ 125 km to <50 km with an anomalously high offset length of ~130 km in average at ~150 mm/yr (Fig. 8c). Non-transform offsets show instead a gradual decrease in both frequency and cumulative offset length with increasing spreading rate (Fig. 8d and e), but the average offsets (Fig. 8f) range between ~4 and 11 km, with no clear dependence on spreading rate. These data also reveal variations in the relative proportions of frequency and length of NTOs vs. transform discontinuities with increasing rate at velocities <80 mm/yr, with higher ratios at faster velocities but with no clear spreading rate dependence (Fig. 8g and h).

These observations indicate that ridge offset age and/or length magnitude alone is insufficient to predict the structural nature of ridge discontinuities. The data shows a systematic spreading rate threshold in the behaviour of different metrics and parameters at a spreading rate of ~80-100 mm/yr, with spreading rate dependence observed more systematically at velocities below this threshold (Figs. 5, 6, 8). The transition between transform vs. non-transform discontinuities does not depend solely on offset magnitude (length and/or age, Fig. 7) or spreading rate (Fig. 8), and additional factors must be considered.

5. Implications of the new global mid-ocean ridge model

5.1. A detailed and global view of the mid-ocean ridge geometry

The geometry and shape of this plate boundary are key features and parameters for understanding the distribution of different processes operating during oceanic lithospheric accretion (e.g., magmatism and volcanism, tectonic deformation and seismicity, hydrothermal circulation and fluxes). The detailed mapping presented here also provides a database that is suitable for local studies (at the scale of ridge segments), in addition to regional or global ones. Fig. 9 shows the spatial differences in identifying divergent plate boundary (including transform and non-transform discontinuities) by MAPRIDGES (this study), Bird [2003] widely used model, and that of Hasterok et al. [2022]. Differences in the mapped mid-ocean ridge position by the above-mentioned models which exceed 10 km are found for ~45% of Bird [2003] plate boundary (Fig. 9b), and for ~18% of that from Hasterok et al. [2022] (Fig. 9c). Along the plate boundary sections that are well mapped, the averages in offset are of ~13.5 and 6.2 km (Fig. 9d), for the Bird [2003] and Hasterok et al. [2022] models when only the well-mapped ridge sections are considered. The maps also show that the sections of plate boundaries with the largest differences concentrate along some of the back-arc basins, while the geometry of the main ridge systems (e.g., Central Indian Ridge or the South American-Antarctic Ridge, Fig. 9a, c) has been improved in the most recent plate boundary models.

The MAPRIDGES divergent plate boundary geometry thus increases

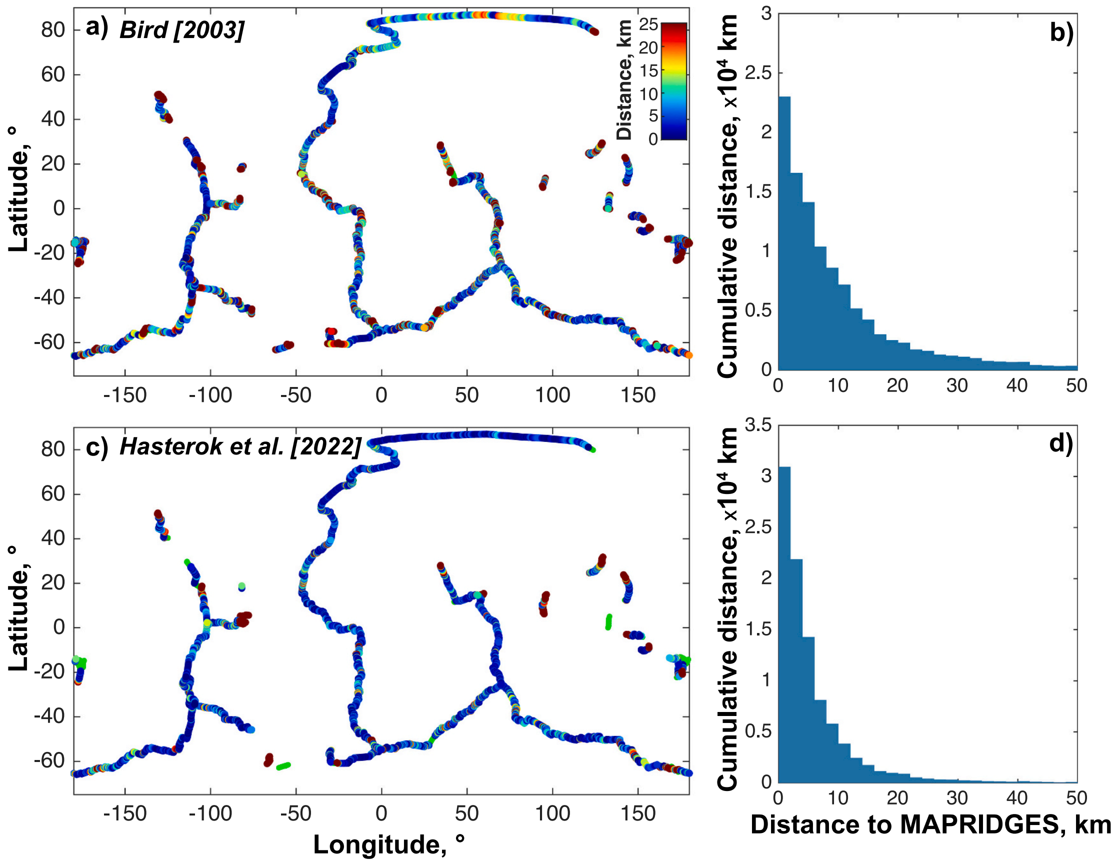

Fig. 9. Spatial differences between the present-day ridge system geometry and divergent boundaries from global plate models from a) and b) Bird [2003] and c) and d) Hasterok et al. [2022] (top and bottom respectively). The histograms in b) and d) show that plate boundary geometry in global models has improved over time, but that spatial offsets can exceed several km to tens of km locally, as shown in Fig. 4.

the accuracy and resolution in the position of the ridge axis, better defining ridge segments and their associated discontinuities. This allows for a precise location of observables (e.g., samples, geological observation, geophysical measurements, seismic activity) relative to individual ridge segments and/or discontinuities. In the case of seismic events, the differences in the position of the plate boundary (~13.5 and 6.2 km for the two models discussed above) are commensurable to the errors of teleseismic events (~10-25 km [e.g., Bondár et al., 2004; Olive and Escartín, 2016]) and those from hydrophone networks (from a few km to >10 km [e.g., Fox et al., 2001; Parnell-Turner et al., 2022]). An accurately defined plate boundary can also be critical for the relocation of teleseismic events (e.g., relative to transform faults [e.g., Janin and Behn, 2026]), or to determine the tectonic context near non-transform discontinuities (e.g., segment center vs. ends, inside vs. outside-corner settings at the end of segments) [e.g., Simão et al., 2010; Zheng et al., 2022]. Defining the ridge axis with higher precision can thus be important for numerous studies, such as determining the width of the actively deforming lithosphere, which is done based on the distribution of seismicity as a function of distance from the ridge axis [e.g., Smith et al., 2003], understanding the links to seismic moment release and spreading rate [e.g., Pinzón and Vargas, 2021], or updating the geometry of tectonic plate models (e.g., GPlates, https://www.gplates.org) that can be used for refining various present-day global flux estimates (volcanism, heat and chemical fluxes [e.g., Merdith et al., 2020]).

5.2. *Stability of ridge discontinuities: transform vs. non-transform offsets*

The formation of transform vs. non-transform discontinuities and their stability along mid-ocean ridges has been studied by analogue, numerical, and analytical thermomechanical models exploring numerous parameters such as spreading rate, regional topographic gradients, ridge obliquity, mantle temperature and melt supply, and the rheology and thermal state of young oceanic lithosphere [e.g., Phipps Morgan and Parmentier, 1985; Lachenbruch and Thompson, 1972; Oldenburg and Brune, 1972; Gerya, 2012; Sibrant et al., 2021; Martinez and Hey, 2022; Su et al., 2026]. These models suggested that the formation of transform faults, overlapping and underlapping NTOs, or their stability depend on competing processes. These include strain weakening mechanisms promoting strain localization, or magmatism coupled with a thin lithosphere at fast-spreading ridges [e.g., Martinez and Hey, 2022], among other processes.

The MAPRIDGES set of ridge discontinuities provides an exhaustive catalogue of ridge discontinuities and associated geometrical parameters (long-axis overlap or underlap, across-axis lateral offset and age offset) to gain further insight in the controls on the nature of ridge discontinuities and ridge segmentation, and the transition between localized and distributed accommodation of deformation. Sibrant et al. [2021] provides an analysis of segmentation style and segment offsets based on analogue modelling, and a parametrization that allows a scaling and direct comparison with observed data from the Earth's ridge system. In their analysis, the parameters considered are the mechanical length scale (Z_m), that depends on the properties of the Earth's or analogue systems, and an axial elastic thickness (Z_{axis}), which depends on mantle temperature and spreading rate, in addition to other Earth's parameters (see Equations 1 through 3 in Sibrant et al. [2021]). A critical elastic thickness, Z_c, (771 m for the Earth's system, see Sibrant et al., 2021) is used to scale models and natural observations, and to compare Z_{axis} to Z_c. Their experiments yield an average segment length of 55 km in the Earth's system, that is constant across all spreading rates and Z_{axis}/Z_c (see Fig. 7 in Sibrant et al. [2021]). This average is

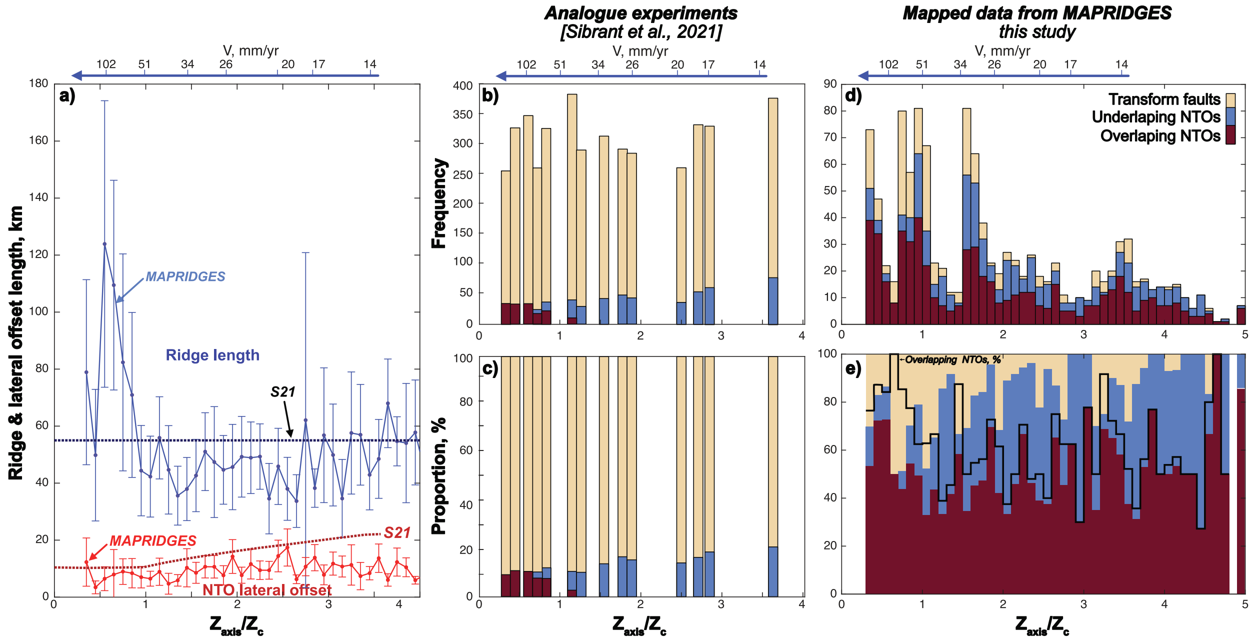

Fig. 10. a) Comparison of MAPRIDGES data (all ridge segments, error bars equal to 1 std) with predictions by Sibrant et al. [2021] (dashed line) as a function of Z_{axis}/Z_c. b) through e) comparison of the distribution of ridge offset types from analogue experiments [Sibrant et al., 2021] (b and c) and from ridge offsets from the MAPRIDGES database (d and e). These distributions are shown as a function of the parameter Z_{axis}/Z_c for both frequency in b) and c), and the relative proportion of discontinuity types, including transforms, overlapping and underlapping NTOs, in b) and d). In d) the black line shows the proportion of NTOs showing an overlapping geometry, excluding transforms. To calculate Z_{axis}/Z_c for the MAPRIDGES dataset we use the spreading rate for each transform and non-transform discontinuity (shown for reference on all panels), and a globally uniform Z_c (see equation 1, and Z_c=771m in Sibrant et al., 2021).

somewhat higher than the average segment length of ~46 km calculated from the MAPRIGDES database. Our analysis shows a mild ridge length increase with increasing spreading rates at velocities less than 80 mm/yr (Fig. 5b), but no clear trend when observed data are reported as a function of the ratio Z_{axis}/Z_c (Fig. 10a). The model of Sibrant et al. [2021] also predicts an increase in the average lateral offset, which varies with Z_{axis}/Z_c at ratios greater than 1. Observations show instead lower predicted values, with no clear dependence on Z_{axis}/Z_c (Fig. 10a).

The analysis of analogue data provides a distribution of discontinuity types that also depends on the ratio Z_{axis}/Z_c (see Fig. 8 in Sibrant et al. [2021]). In particular, overlapping spreading centres (corresponding to overlapping NTOs in this study), are observed at $Z_{axis}/Z_c<1$, and would correspond to the OSCs common at fast-spreading centres (Fig. 10 b and c). underlapping discontinuities (equivalent to non-transform, non-overlapping offsets or NTNOOs in Sibrant et al. [2021]) fall primarily at $Z_{axis}/Z_c>1$ and increase in relative proportion (Fig. 10b, c). The mapped data used in MAPRIDGES (Fig. 10d, e) show instead that overlapping discontinuities are observed at all ratios of Z_{axis}/Z_c and are not restricted to $Z_{axis}/Z_c<1$. Underlapping discontinuities occur at all ratios of Z_{axis}/Z_c including at $Z_{axis}/Z_c<1$, with a small increase with increasing Z_{axis}/Z_c (Fig. 10e). Finally, the proportion of transform faults in the observed data is significantly lower that from the analogue experiments (Fig. 10b-e).

We document differences between averages of segment length, lateral offset length, and distribution of discontinuity types between observations, analogue experiments and model predictions. These discrepancies suggest that, in addition to spreading rate, other parameters control the mechanical properties of the lithosphere along the axis or ridge segments (i.e., the axial elastic skin thickness, Z_{axis}). A first difference between natural, analogue and models is the mantle temperature, assumed here to be constant (T_m=1400°C) to calculate Z_{axis} (Equation 1 Sibrant et al. [2021]), varies along the global mid-ocean ridge system. Estimates from a combination of mid-ocean ridge depth, seismic velocity and geochemistry, suggest variations that T_m varies between ~1320°C and ~1470°C [e.g., Dalton et al., 2014]. These modest variations in absolute mantle temperature have a minor impact in Z_{axis} estimates would not result in a noticeable difference in the global distributions shown in Fig. 10d-e [Sibrant et al., 2021]. The critical axial thickness also depends on other parameters such as thermal diffusivity and other mechanical properties of the lithosphere such as fracture toughness and yield stress (Eq. 2 in Sibrant et al. [2021]). These parameters may vary among segments owing to presence of melt, presence of different lithologies such as serpentinite modifying the mechanical properties, variations in permeability of the brittle lithosphere impacting diffusivity, etc.

Geological complexity of natural systems, that will impact the different parameters mentioned above, is not captured by analogue experiments and models, nor by the outlined parametrization. There are no global observations or proxies to evaluate these parameters along the full mid-ocean ridge system. We thus speculate that a significant portion of the discrepancies between models [Sibrant et al., 2018] and parameters derived from the MAPRIDGES dataset may be attributed to variations in these mechanical and physical properties under the ridge axis. There are profound differences in the mode of accretion of the oceanic lithosphere, and in particular the formation of a fully magmatic crust (fast spreading ridges, slow spreading ridges with robust melt supply) vs. a lithosphere that includes both magmatic and mantle material [e.g., Cannat, 1993; Cannat et al., 2006; Escartín et al., 2008; Olive and Dublanchet, 2020]. Notably, slow- and intermediate spreading ridges (spreading rates less than 80 mm/yr) display a wide range of ridge morphologies that vary from amagmatic extension (e.g., sections of the Southwest Indian Ridge [Cannat et al., 2006]) to axial highs reminiscent of fast-spreading ridges (e.g., Reykjanes Ridge near Iceland [Keeton et al., 1997]). Furthermore, a single segment may show significant variations along its axis in the mode of accretion, a complexity that the analyses presented above may not capture as the parameters are assigned to the whole segment. To better understand and explain the variability and patterns observed in the natural system and shown in this study, a global analysis should include a classification of both ridge segments and non-transform offsets in terms of mode of accretion [e.g., Cannat et al., 2006; Olive and Dublanchet, 2020], and an evaluation of the along-axis variations that may impact these analyses. They should be associated with parameters such as spreading, and mechanical properties of the lithosphere, controlled by composition that may be variable across different modes of accretion (e.g., presence of serpentinites and degree of lithospheric alteration, proportion of magmatic vs. mantle rocks); these parameters partially independent of both spreading rate and mantle temperature.

5.3. *Modification of the oceanic lithosphere at non-transform discontinuities*

The length of the mid-ocean ridge system has been a critical parameter for global studies of lithospheric accretion and related to ridge processes. These include magma production and estimates of volcanic activity with associated degassing CO_2 or He [e.g., Resing et al., 2004; Burley and Katz, 2015; Le Voyer et al., 2019]. Fluid circulation also results in exchanges with the overlying ocean [e.g., Müller et al., 2013]. A consequence of this circulation is the hydration of ultramafic rocks and the production of CH_4 and H_2, that can be calculated based on assumptions including ridge length, lithospheric thickness, and degree of serpentinization [e.g., Baker et al., 1996; Elderfield and Schulz, 1996; Alt, 2003; Cannat et al., 2010]. Recent studies show that fracture zones are portions of divergent plate boundaries that can be significant contributors to these fluxes. Crustal thinning and reduction of mantle velocities attributed to serpentinization are observed in the seismic structure of transform faults [e.g., Detrick et al., 1990, 1993], which, supported by geological and geophysical data, provide evidence of fluid circulation and hydration [Prigent et al., 2020; Chesley et al., 2025]. Recent models suggest for example that flux of hydrogen or methane linked to serpentinization from fracture zones may be commensurable to that of spreading ridge segments [Rüpke and Hasenclever, 2017], and these structures have been incorporated in recent models of lithospheric alteration and methane production [Merdith et al., 2020]. Further studies also suggest that transform faults may lead to secondary volcanism [e.g., Guo et al., 2023], and be linked to transform-related magmatism and volcanism [Grevemeyer et al., 2021; Tian et al., 2024]. These observations suggests that transform faults host active magmatic processes distinct from those at adjacent ridge segments, impacting the lithosphere in the immediate vicinity of these structures and that was previously formed along the ridge axis.

Fig. 11 illustrates different processes operating at NTOs that may both modify the structure and composition of the oceanic lithosphere formed on axis, and illustrated by the differences between the panels on the left (NTO-affected lithosphere) with respect to the panels on the right ('normal' lithosphere that is not affected by NTO processes). At slow-spreading ridges, associated with a heterogenous crust, NTOs often display a thinner crust and reduced melt supply at slow-spreading ridges [e.g., Kuo and Forsyth, 1988; Detrick et al., 1995], often showing extensional deformation linked to high levels of seismicity [e.g., Tsang-Hin-Sun et al., 2016; deMartin et al., 2007], tectonic uplift and evidence of methane outflow linked to alteration and serpentinization [e.g.,

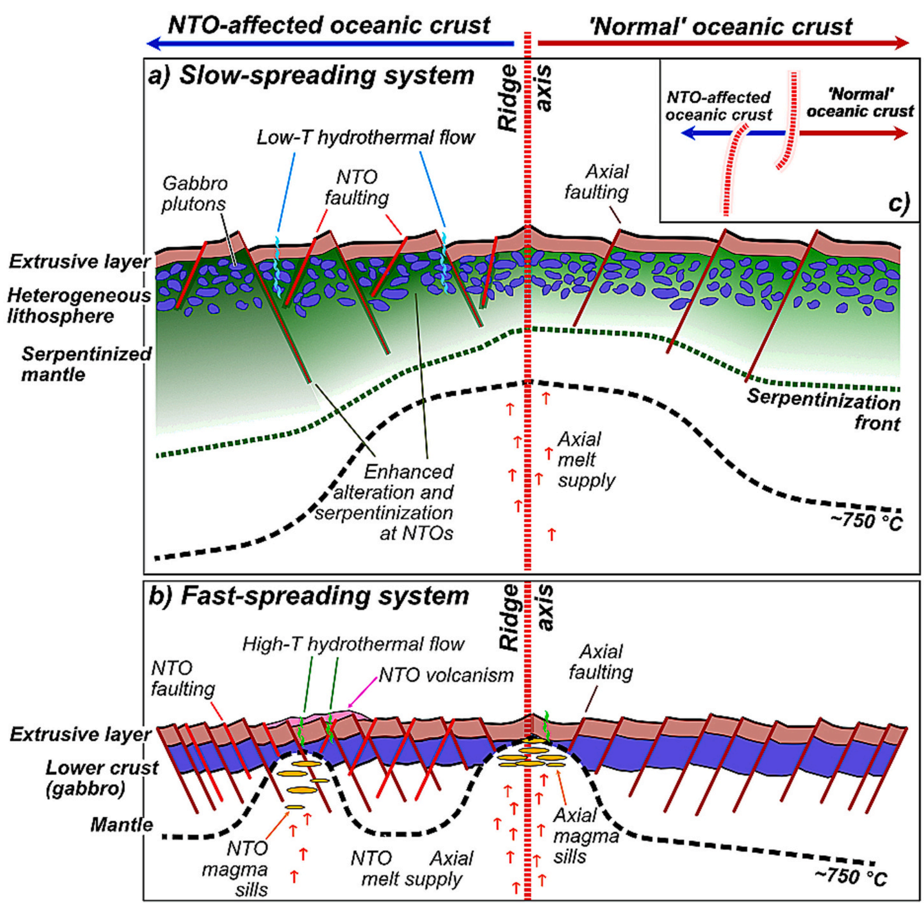

Fig. 11. Modification of the oceanic lithosphere by processes operating at non-transform offsets. a) Across-axis section of a slow spreading system, associated with a compositionally heterogeneous lithosphere and associated with a discontinuous crust [e.g., Cannat, 1993] showing enhancement of alteration (serpentinization) linked to low-temperature hydrothermal circulation, in addition to NTO-related faulting, and associated with an overall colder lithosphere than on the conjugate flank, that is formed on-axis, preserved and rafted off-axis. b) Across axis section of a fast-spreading system, showing instead magmatic processes linked to the NTO and adjacent ridge segment end, with NTO-related magmatism and associated volcanic eruptions and deformation over imprinting the structure of the oceanic lithosphere acquired on-axis. In this case the oceanic crust is magmatic, homogeneous, and continuous.

Spencer et al., 1997; Gràcia et al., 2000]. Circulation of low-temperature fluids may contribute to serpentinization both widespread throughout the lithosphere, and enhanced along pre-existing and newly-formed faults (Fig. 11a), and thus impacting locally the composition, structure, and temporal variations of the lithosphere [e.g., Cannat et al., 1995; Zhang et al., 2018]. NTOs at slow-spreading segments may also show evidence of magmatic activity and linked to high-temperature fluid circulation (not depicted in Fig. 11a) hence modifying the structure and composition of the lithosphere while enhancing serpentinization [e.g., Andreani et al., 2014; Canales et al., 2017]. This is shown in Fig. 11a by a deepening of the isotherms, a higher degree of serpentinization, faulting linked to the overlapping segment, and the occurrence of low-temperature fluid flow at the NTO-affected oceanic lithosphere relative to the conjugate flank.

In contrast, at fast-spreading ridges (Fig. 11b), the lithosphere within overlapping NTOs may undergo block rotation, late magmatic reactivation and volcanism often cross-cutting prior seafloor textures, reactivating high-temperature fluid circulation [e.g., Tyler et al., 2007], and impacting significant portions of the seafloor [e.g., Macdonald and Fox, 1983; Wilson, 1990]. This is depicted in Fig. 11b by NTO-related faulting, emplacement of magma sills with associated volcanic eruptions, and the reactivation of high-temperature hydrothermal activity at the oceanic lithosphere impacted by NTO processes, and relative to the conjugate flank rafted off-axis.

The contribution of non-transform offsets to active processes along divergent margins relative to ridge segments and transform faults was neither identified nor quantified in prior studies. Based on the measured lateral and along-axis offsets, non-transform offsets are an overlooked component of these active boundaries, that can significantly contribute to the active processes mentioned above. Firstly, the cumulative lateral offset of NTOs is about 30% of that of transform faults globally (Table 2), with a higher percentage for slow spreading rates (Fig. 8g, h). Secondly, the cumulative along-axis offset corresponds to ca. 10% of the total ridge length globally, (Table 2) and as in the case of the lateral offset, the cumulative length of these along-axis offsets increases with decreasing spreading rate (Fig. 6c). It follows that at slow spreading ridges, and in the presence of a heterogenous lithosphere containing peridotite [e.g., Cannat, 1993], distributed deformation in the non-transform zone can promote circulation of fluids and enhance serpentinization. This is supported by the observation of higher levels of seismic activity at segment ends adjacent to NTOs relative to segment centers [e.g., Tsang-Hin-Sun et al., 2016], that also host methane plumes and hydrothermal systems [e.g., Gràcia et al., 2000]. Based on the published rates of serpentinization and associated fluxes of hydrogen [Rüpke and Hasenclever, 2017] and methane [Merdith et al., 2020], the contribution of NTOs to these fluxes may be a significant fraction of that associated with ridges and fracture zones.

6. Conclusions

From the interpretation of available multibeam bathymetry and the digitization of oceanic plate boundaries, the MAPRIDGES database provides a comprehensive, global, and detailed dataset reporting individual ridge segments, transform faults, and non-transform offsets, based on the interpretation of available multibeam bathymetry and the digitization of these structures. The global mid-ocean ridge system shows a total length of ~71200 km, with less than 25% of its length unmapped or poorly surveyed. We present an exhaustive catalogue of 262 transform faults and 10 transform zones, that have a cumulative length of 28200 km. In this study we also provide a first and global quantification of non-transform discontinuities, both overlapping and underlapping. These structures accumulate ~6500 km of along-axis offset, that result in a corrected ridge length of 67900 km, once these overlaps and underlaps are accounted for. Non-transform discontinuities accumulate a total lateral offset of ~9000 km, representing about one-third of the total transform offset (~28300 km). The total mid-ocean ridge plate boundary thus is calculated at ~105400 km, including ~37500 km of lateral offset boundaries that are active. These zones host active processes, including magmatism, volcanism, deformation, fluid circulation and alteration, that modify the oceanic lithosphere formed along adjacent ridge segments.

The MAPRIDGES data shows that characteristics of NTOs for spreading rates less than 80-100 mm/yr are different from the ones developed at higher spreading rates. At spreading rates below the 80-100 mm/yr threshold, the amount of overlapping ridge offsets increases, the cumulative lateral offset of NTOs overall decreases, and the cumulative length of transform faults is relatively constant. Above this threshold, these relationships with spreading rate break down. Lateral offset of transform and NTOs overlap at all length scales, with numerous transforms observed at less than 30 km with lengths as short as ~10 km, while several NTOs display lengths exceeding 50 km. These observations, together with comparisons with analogue experiments results and model predictions, indicate that segmentation and nature of ridge discontinuities are modulated only partially by spreading rate and mantle temperature and other processes may be active in these regions. Understanding the natural distribution of ridge segments and discontinuities, together with their geometry (lengths, offsets) thus requires an analysis that incorporates a geological classification of these structures related to the mode of accretion, and the rheology of the lithosphere based on resulting composition.

Finally, a global analysis of non-transform offset characteristics and distributions suggests these features play an overlooked role in the modification of oceanic lithosphere. We expect that at least 10% of the oceanic lithosphere is modified post-accretion along these structures, through a combination of processes that include active tectonic deformation, magmatic intrusion and volcanism, hydrothermal circulation and alteration. With a cumulative offset length of ~30% of that of transform faults, non-transform offsets should be included in studies of global budgets of fluid flow and associated chemical and heat fluxes. These discontinuities and their geometry will also facilitate the quantification of deformation and improve the understanding of seismicity budgets though a differentiation of seismic events along ridges (linked to accretion) and discontinuities (linked to off-axis deformation).

Declaration of competing interest

The authors declare that they have no known competing financial interests or personal relationships that could have appeared to influence the work reported in this paper.

Acknowledgements

This study has been partially supported by the Commission for the Geological Map of the World (to BS & M. Pubellier), and by the project ANR DYHAM (Ref. ANR-23-CE01-0011-01 to JE). CG acknowledges financial support by the Research Council of Norway through its Centres of Excellence Scheme, project numbers 332523 (PHAB) and thanks the School of Earth and Planetary Sciences (EPS), Curtin University, for hosting her while working on this paper. This paper benefitted from the open-source QGIS software used to digitize features in the database, and to draft the maps in this paper.

Appendix A. Supplementary data

Supplementary data to this article can be found online at https://doi.org/10.1016/j.earscirev.2026.105633.

Data availability

The MAPRIGES database is available on-line and in open access at the SEANOE data repository (https://seanoe.org; https://doi.org/10.17882/99981, Sautter et al. [2024]). This database will be updated as new datasets and corrections are available.

References

Abelson, M., Anon, A., 1997. Mechanics of oblique spreading and ridge segmentation. Earth Planet. Sci. Lett. 148 (3–4), 405–421. https://doi.org/10.1016/S0012-821X(97)00054-X.

Alt, J.C., 2003. Hydrothermal fluxes at mid-ocean ridges and on ridge flanks. Compt. Rendus Géosci. 335 (10–11), 853–864. https://doi.org/10.1016/j.crte.2003.02.001.

Andreani, M., Escartin, J., Delacour, A., Ildefonse, B., Godard, M., Dyment, J., Fallick, A. E., Fouquet, Y., 2014. Tectonic structure, lithology, and hydrothermal signature of the Rainbow massif (Mid-Atlantic Ridge 36°14′N). Geochem. Geophys. Geosyst. 15, 3543–3571. https://doi.org/10.1002/2014GC005269.

Augustin, N., van der Zwan, F.M., Devey, C.W., Ligi, M., Kwasnitschka, T., Feldens, P., Bantan, R.A., Basaham, A.S., 2016. Geomorphology of the central Red Sea Rift: determining spreading processes. Geomorphology 274, 162–179. https://doi.org/10.1016/j.geomorph.2016.08.028.

Baker, E., 2007. Hydrothermal cooling of midocean ridge axes: Do measured and modeled heat fluxes agree? Earth Planet. Sci. Lett. 263 (1–2), 140–150. https://doi.org/10.1016/j.epsl.2007.09.010.

Baker, E.T., Chen, Y.J., Phipps Morgan, J., 1996. The relationship between near-axis hydrothermal cooling and the spreading rate of mid-ocean ridges. Earth Planet. Sci. Lett. 142, 137–145.

Bellahsen, N., Husson, L., Autin, J., Leroy, S., D'Acremont, E., 2013. The effect of thermal weakening and buoyancy forces on rift localization: field evidences from the Gulf of Aden oblique rifting. Tectonophysics 607, 80–97. https://doi.org/10.1016/j.tecto.2013.05.042.

Bird, P., 2003. An updated digital model of plate boundaries. Geochem. Geophys. Geosyst. 4 (3). https://doi.org/10.1029/2001GC000252.

Bonatti, E., Brunelli, D., Buck, W., Cipriani, A., Fabretti, P., Ferrante, V., Gasperini, L., Ligi, M., 2005. Flexural uplift of a lithospheric slab near the Vema transform (Central Atlantic): timing and mechanisms. Earth Planet. Sci. Lett. 240 (3–4), 642–655. https://doi.org/10.1016/j.epsl.2005.10.010.

Bondár, I., Myers, S.C., Engdahl, E.R., Bergman, E.A., 2004. Epicentre accuracy based on seismic network criteria. Geophys. J. Int. 156 (3), 483–496. https://doi.org/10.1111/j.1365-246X.2004.02070.x.

Burley, J.M.A., Katz, R.F., 2015. Variations in mid-ocean ridge CO2 emissions driven by glacial cycles. Earth Planet. Sci. Lett. 426, 246–258. https://doi.org/10.1016/j.epsl.2015.06.031.

Canales, J.P., Dunn, R.A., Arai, R., Sohn, R.A., 2017. Seismic imaging of magma sills beneath an ultramafic-hosted hydrothermal system. Geology 45 (5), 451–454. https://doi.org/10.1130/G38795.1.

Cann, J.R., Smith, D.K., Escartín, J., Schouten, H., 2015. Tectonic evolution of 200 km of Mid-Atlantic Ridge over 10 million years: interplay of volcanism and faulting. Geochem. Geophys. Geosyst. 16 (7), 2303–2321. https://doi.org/10.1002/2015GC005797.

Cannat, M., 1993. Emplacement of mantle rocks in the seafloor at mid-ocean ridges. J. Geophys. Res. Solid Earth 98 (B3), 4163–4172. https://doi.org/10.1029/92JB02221.

Cannat, M., Fontaine, F.J., Escartin, J., Rona, P., Devey, C.W., Dyment, J., Murton, B., 2010. Serpentinization and Associated Hydrogen and Methane Fluxes at Slow Spreading Ridges. In: Diversity of Hydrothermal Sytems on Slow Spreading Ocean Ridges. AGU, Washington DC, pp. 43–66.

Cannat, M., Mével, C., Maia, M., Deplus, C., Durand, C., Gente, P., Agrinier, P., Belarouchi, A., Dubuisson, G., Humler, E., Reynolds, J., 1995. Thin crust, ultramafic exposures, and rugged faulting patterns at the Mid-Atlantic Ridge (22°-24°N). Geology 23 (1), 49–52.

Cannat, M., Sauter, D., Mendel, V., Ruellan, E., Okino, K., Escartín, J., Combier, V., Baala, M., 2006. Modes of seafloor generation at a melt-poor ultraslow-spreading ridge. Geology 34 (7), 605. https://doi.org/10.1130/G22486.1.

Cao, X., Collins, A.S., Pisarevsky, S., Flament, N., Li, S., Hasterok, D., Müller, R.D., 2024. Earth's tectonic and plate boundary evolution over 1.8 billion years. Geosci. Front. 15 (6), 101922. https://doi.org/10.1016/j.gsf.2024.101922.

Carbotte, S.M., Smith, D.K., Cannat, M., Klein, E.M., 2015. Tectonic and Magmatic Segmentation of the Global Ocean Ridge System: A Synthesis of Observations: Geological Society. Special Publications, London. https://doi.org/10.1144/SP420.5.

Chen, J., Olive, J., Cannat, M., 2023. Beyond spreading rate: controls on the thermal regime of mid-ocean ridges. Proc. Natl. Acad. Sci. 120 (45), 1–9. https://doi.org/10.1073/pnas.2306466120.

Chesley, C., Evans, R., Warren, J.M., Gase, A.C., Perez, J., Armerding, C., Brewer, H., Koenig, P., Attias, E., Fluegel, B.L., Kim, J.-D., Hummel, N., Enright, K., Topp-Johnson, E., et al., 2025. Evidence for crustal brines and deep fluid infiltration in an oceanic transform fault. Sci. Adv. 11 (15), 1–10. https://doi.org/10.1126/sciadv.adu3661.

Cogné, J.-P., Humler, E., 2004. Temporal variation of oceanic spreading and crustal production rates during the last 180 My. Earth Planet. Sci. Lett. 227 (3–4), 427–439. https://doi.org/10.1016/j.epsl.2004.09.002.

Cowan, D.S., Botros, M., Johnson, H.P., 1986. Bookshelf tectonics: Rotated crustal blocks within the Sovanco Fracture Zone. Geophys. Res. Lett. 13 (10), 995–998. https://doi.org/10.1029/GL013i010p00995.

Dalton, C.A., Langmuir, C.H., Gale, A., 2014. Geophysical and geochemical evidence for deep temperature variations beneath Mid-Ocean Ridges. Science 344 (6179), 80–83. https://doi.org/10.1126/science.1249466.

Dauteuil, O., Bourgeois, O., Mauduit, T., 2002. Lithosphere strength controls oceanic transform zone structure: insights from analogue models. Geophys. J. Int. 150 (3), 706–714. https://doi.org/10.1046/j.1365-246X.2002.01736.x.

deMartin, B.J., Sohn, R.A., Pablo Canales, J., Humphris, S.E., 2007. Kinematics and geometry of active detachment faulting beneath the Trans-Atlantic Geotraverse (TAG) hydrothermal field on the Mid-Atlantic Ridge. Geology 35, 8, 711. https://doi.org/10.1130/G23718A.1.

DeMets, D.C., Gordon, R.G., Argus, D.F., 2010. Geologically current plate motions. Geophys. J. Int. 181, 1–80. https://doi.org/10.1111/j.1365-246X.2010.04491.x.

Detrick, R.S., Mutter, J.C., Buhl, P., Kim, I.I., 1990. No evidence from multichannel reflection data for a crustal magma chamber in the MARK area on the Mid-Atlntic Ridge. Nature 347, 61–64.

Detrick, R.S., White, R.S., Purdy, G.M., 1993. Crustal structure of North-Atlantic fracture zones. Rev. Geophys. 31 (4), 439–459.

Detrick, R.S., Needham, H.D., Renard, V., 1995. Gravity anomalies and crustal thickness variations along the Mid-Atlantic Ridge between 33°N and 40°N. J. Geophys. Res. Solid Earth 100 (B3), 3767–3787. https://doi.org/10.1029/94JB02649.

Elderfield, H., Schulz, A., 1996. Mid-Ocean ridge hydrothermal fluxes and the chemical composition of the ocean. Annu. Rev. Earth Planet. Sci. 24, 191–224.

Escartín, J., Olive, J.-A., 2022. Mid-Ocean Ridges and their geomorphological features. In: Treatise on Geomorphology. Elsevier, pp. 847–881.

Escartín, J., Smith, D.K., Cann, J., Schouten, H., Langmuir, C.H., Escrig, S., 2008. Central role of detachment faults in accretion of slow-spreading oceanic lithosphere. Nature 455 (7214), 790–794. https://doi.org/10.1038/nature07333.

Ewing, M., Heezen, B.C., 2013. Some Problems of Antarctic Submarine Geology, pp. 75–81. https://doi.org/10.1029/GM001p0075.

Fournier, M., Bellahsen, N., Fabbri, O., Gunnel, Y., 2004. Oblique rifting and segmentation of the NE Gulf of Aden passive margin. Geochem. Geophys. Geosyst. 5 (11), Q11005. https://doi.org/10.1029/2004GC000731.

Fox, C.G., Matsumoto, H., Lan, T.-K.A., 2001. Monitoring Pacific Ocean seismicity from an autonomous hydrophone array. J. Geophys. Res. 106 (B3), 4183–4206.

Gale, A., Langmuir, C.H., Dalton, C.A., 2014. The global systematics of Ocean Ridge Basalts and their origin. J. Petrol. 55 (6), 1051–1082. https://doi.org/10.1093/petrology/egu017.

GEBCO, 2024. Compilation Group 2024. https://doi.org/10.5285/1c44ce99-0a0d-5f4f-e063-7086abc0ea0f.

Gerya, T., 2012. Origin and models of oceanic transform faults. Tectonophysics 522–523, 34–54. https://doi.org/10.1016/j.tecto.2011.07.006.

Goff, J.A., 2020. Identifying characteristic and anomalous mantle from the complex relationship between Abyssal Hill roughness and spreading rates. Geophys. Res. Lett. 47 (11), 1–9. https://doi.org/10.1029/2020GL088162.

Gordon, R.G., 1998. The plate tectonic approximation: plate nonrigidity, diffuse plate boundaries, and global plate reconstructions. An. Rev. Earth. Planet. Sci. 26, 615–642. https://doi.org/10.1146/annurev.earth.26.1.615.

Gràcia, E., Charlou, J.L., Radford-Knoery, J., Parson, L.M., 2000. Non-transform offsets along the Mid-Atlantic Ridge south of the Azores (38°N–34°N): ultramafic exposures and hosting of hydrothermal vents. Earth Planet. Sci. Lett. 177 (1–2), 89–103. https://doi.org/10.1016/S0012-821X(00)00034-0.

Grevemeyer, I., Rüpke, L.H., Morgan, J.P., Iyer, K., Devey, C.W., 2021. Extensional tectonics and two-stage crustal accretion at oceanic transform faults. Nature 591 (7850), 402–407. https://doi.org/10.1038/s41586-021-03278-9.

Grindlay, N.R., Fox, P.J., 1993. Lithospheric stresses associated with non-transform offsets of the Mid-Atlantic Ridge: implications for a finite element analysis. Tectonics 12 (4), 982–1003.

Guo, Z., Liu, S., Rüpke, L., Grevemeyer, I., Morgan, J.P., Lange, D., Ren, Y., Tao, C., 2023. Disparate crustal thicknesses beneath oceanic transform faults and adjacent fracture zones revealed by gravity anomalies. Geology 51 (3), 300–304. https://doi.org/10.1130/G50429.1.

Harper, H., Luttrell, K., Sandwell, D.T., 2023. Ridge propagation and the stability of small mid-ocean ridge offsets. J. Geophys. Res. Solid Earth 128 (8). https://doi.org/10.1029/2023JB027443.

Hasterok, D., Halpin, J.A., Collins, A.S., Hand, M., Kreemer, C., Gard, M.G., Glorie, S., 2022. New maps of global geological provinces and tectonic plates. Earth Sci. Rev. 231 (May), 104069. https://doi.org/10.1016/j.earscirev.2022.104069.

Hensen, C., Duarte, J.C., Vannucchi, P., Mazzini, A., Lever, M.A., Terrinha, P., Géli, L., Henry, P., Villinger, H., Morgan, J., Schmidt, M., Gutscher, M.-A., Bartolome, R., Tomonaga, Y., et al., 2019. Marine transform faults and fracture zones: a joint perspective integrating seismicity, fluid flow and life. Front. Earth Sci. 7 (March), 1–29. https://doi.org/10.3389/feart.2019.00039.

Hey, R., 1977. A new class of "pseudofaults" and their bearing on plate tectonics: a propagating rift model. Earth Planet. Sci. Lett. 37 (2), 321–325. https://doi.org/10.1016/0012-821X(77)90177-7.

Izzeldin, A.Y., Mitchell, N.C., 2024. Shield suture zones control positions of oceanic spreading segment discontinuities in the central Red Sea. In: Rasul, N.M.A., Stewart, I.C.F. (Eds.), Rifting and sediments in the Red Sea and Arabian Gulf regions. Taylor and Francis, London, pp. 61–74. https://doi.org/10.1201/9781003321415-5.

Jakobsson, M., Mohammad, R., Karlsson, M., et al., 2024. The international bathymetric chart of the Arctic Ocean version 5.0. Sci. Data 11, 1420. https://doi.org/10.1038/s41597-024-04278-w.

Janin, A., Behn, M.D., 2026. faults revealed by teleseismic earthquake focal mechanisms. Geophys. J. Int. 245, 1–49. https://doi.org/10.1093/gji/ggag078.

Kappel, E.S., Ryan, W.B.F., 1986. Volcanic episodicity and a non-steady-state rift valley along northeast Pacific spreading centers: evidence from SeaMARC I. J. Geophys. Res. 91, 13925–13940. https://doi.org/10.1029/JB092iB08p08089.

Keeton, J.A., Searle, R.C., Parsons, B., White, R.S., Murton, B.J., Parsons, L.M., Peirce, C., Sinha, M., 1997. Bathymetry of the Reykjanes Ridge. Mar. Geophys. Res. 19, 55–64. https://doi.org/10.1023/A:1004266721393.

Klein, E.M., Langmuir, C.H., 1987. Global correlations of ocean ridge basalt chemistry with axial depth and crustal thickness. J. Geophys. Res. 92, 8089–8115n. https://doi.org/10.1029/JB092iB08p08089.

Kreemer, C., Blewitt, G., Klein, E.C., 2014. A geodetic plate motion and global strain rate model. Geochem. Geophys. Geosyst. 15, 3849–3889. https://doi.org/10.1002/2014GC005407.

Kuo, B.-Y., Forsyth, D.W., 1988. Gravity anomalies of the ridge-transform system in the South Atlantic between 31 and 34.5°S: upwelling centers and variations in crustal thickness. Mar. Geophys. Res. 10 (3–4), 205–232. https://doi.org/10.1007/BF00310065.

Lachenbruch, A.H., Thompson, G.A., 1972. Oceanic ridges and transform faults: their intersection and resistance to plate motions. Earth Planet. Sci. Lett. 15, 116–122.

Le Voyer, M., Hauri, E.H., Cottrell, E., Kelley, K.A., Salters, V.J.M., Langmuir, C.H., Hilton, D.R., Barry, P.H., Füri, E., 2019. Carbon fluxes and primary magma CO2 contents along the global mid-ocean ridge system. Geochem. Geophys. Geosyst. 20 (3), 1387–1424. https://doi.org/10.1029/2018GC007630.

Lin, J., Purdy, G.M., Schouten, H., Sempéré, J.-C., Zervas, C., 1990. Evidence from gravity data for focused magmatic accretion along the Mid-Atlantic Ridge. Nature 344 (6267), 627–632. https://doi.org/10.1038/344627a0.

Lodolo, E., Coren, F., Ben-Avraham, Z., 2013. How do long-offset oceanic transforms adapt to plate motion changes? The example of the Western Pacific-Antarctic plate boundary. J. Geophys. Res. Solid Earth 118 (3), 1195–1202. https://doi.org/10.1002/jgrb.50109.

Macdonald, K.C., 1982. Mid-Ocean Ridges: fine scale tectonic, volcanic and hydrothermal processes within the plate boundary zone. Annu. Rev. Earth Planet. Sci. 10 (1), 155–190. https://doi.org/10.1146/annurev.ea.10.050182.001103.

Macdonald, K.C., Fox, P.J., 1983. Overlapping spreading centres: new accretion geometry on the East Pacific Rise. Nature 302 (5903), 55–58. https://doi.org/10.1038/302055a0.

Macdonald, K.C., Scheirer, D.S., Carbotte, S.M., 1991. Mid- Ocean ridges: Discontinuities, segments and giant cracks. Science 253, 986–994.

Macdonald, K.C., Fox, P.J., Alexander, R.T., Pockalny, R., Gente, P., 1996. Volcanic growth faults and the origin of Pacific abyssal hills. Nature 380 (6570), 125–129. https://doi.org/10.1038/380125a0.

Martinez, F., Hey, R., 2022. Mantle melting, lithospheric strength and transform fault stability: Insights from the North Atlantic. Earth Planet. Sci. Lett. 579, 117351. https://doi.org/10.1016/j.epsl.2021.117351.

Matthews, K.J., Maloney, K.T., Zahirovic, S., Williams, S.E., Seton, M., Müller, R.D., 2016. Global plate boundary evolution and kinematics since the late Paleozoic. Glob. Planet. Chang. 146, 226–250. https://doi.org/10.1016/j.gloplacha.2016.10.002.

McGuire, J.J., Collins, J.A., Gouédard, P., Roland, E., Lizarralde, D., Boettcher, M.S., Behn, M.D., van der Hilst, R.D., 2012. Variations in earthquake rupture properties along the Gofar transform fault, East Pacific Rise. Nat. Geosci. 5 (5), 336–341. https://doi.org/10.1038/ngeo1454.

Menard, H.W., 1961. The East Pacific Rise. Sci. Am. 205 (6), 52–61. https://doi.org/10.1038/scientificamerican1261-52.

Menard, H.W., 1965. The world-wide oceanic rise-ridge system. Philos. Trans. R. Soc. Lond. A 258 (1088), 109–122.

Menard, H.W., Atwater, T., 1969. Origin of fracture zone topography. Nature 222, 1037–1040.

Merdith, A.S., Real, P.G., Daniel, I., Andreani, M., Wright, N.M., Coltice, N., 2020. Pulsated global hydrogen and methane flux at Mid-Ocean Ridges driven by pangea breakup. Geochem. Geophys. Geosyst. 21 (4), 1–20. https://doi.org/10.1029/2019GC008869.

Müller, R.D., Roest, W.R., Royer, J.Y., Gahagan, L.M., Sclater, J.G., 1997. Digital isochrons of the world's ocean floor. J. Geophys. Res. Solid Earth 102 (B2), 3211–3214. https://doi.org/10.1029/96jb01781.

Müller, R.D., Sdrolias, M., Gaina, C., Roest, W.R., 2008. Age, spreading rates, and spreading asymmetry of the world's ocean crust. Geochem. Geophys. Geosyst. 9 (4), Q04006. https://doi.org/10.1029/2007GC001743.

Müller, R.D., Dutkiewicz, A., Seton, M., Gaina, C., 2013. Seawater chemistry driven by supercontinent assembly, breakup, and dispersal. Geology 41 (8), 907–910. https://doi.org/10.1130/G34405.1.

Müller, R.D., Zahirovic, S., Williams, S.E., Cannon, J., Seton, M., Bower, D.J., Tetley, M. G., Heine, C., Le Breton, E., Liu, S., Russell, S.H.J., Yang, T., Leonard, J., Gurnis, M., 2019. A global plate model including lithospheric deformation along major rifts and orogens since the Triassic. Tectonics 38 (6), 1884–1907. https://doi.org/10.1029/2018TC005462.

Murton, B.J., Parson, L.M., 1993. Segmentation, volcanism and deformation of oblique spreading centres: a quantitative study of the Reykjanes Ridge. Tectonophysics 222, 237–257.

Murton, B.J., Rona, P.A., 2015. Carlsberg ridge and Mid-Atlantic Ridge: comparison of slow spreading centre analogues. Deep-Sea Res. II Top. Stud. Oceanogr. 121, 71–84. https://doi.org/10.1016/j.dsr2.2015.04.021.

Mutter, J.C., Karson, J.A., 1992. Structural processes at slow-spreading ridges. Science 257 (5070), 627–634. https://doi.org/10.1126/science.257.5070.627.

Naar, D.F., Hey, R.N., 1989. Speed limit for oceanic transform faults. Geology 17 (5), 420. https://doi.org/10.1130/0091-7613(1989)017<0420:SLFOTF>2.3.CO;2.

Nishimura, S., Hashimoto, M., Ando, M., 2004. A rigid block rotation model for the GPS derived velocity field along the Ryukyu arc. Phys. Earth Planet. Inter. 142 (3–4), 185–203. https://doi.org/10.1016/j.pepi.2003.12.014.

Oldenburg, D.W., Brune, J.N., 1972. Ridge transform fault spreading pattern in freezing wax. Science 178 (4058), 301–304. https://doi.org/10.1126/science.178.4058.301.

Oldenburg, D.W., Brune, J.N., 1975. An explanation for the orthogonality of ocean ridges and transform faults. J. Geophys. Res. 80 (17), 2575–2585. https://doi.org/10.1029/JB080i017p02575.

Olive, J., Dublanchet, P., 2020. Controls on the magmatic fraction of extension at mid-ocean ridges. Earth Planet. Sci. Lett. 549, 116541. https://doi.org/10.1016/j.epsl.2020.116541.

Olive, J.-A., Escartín, J., 2016. Dependence of seismic coupling on normal fault style along the Northern Mid-Atlantic Ridge. Geochem. Geophys. Geosyst. 15 (4), 1009–1020. https://doi.org/10.1002/2016GC006460.

Olive, J.A., Behn, M.D., Ito, G., Buck, W.R., Escartín, J., Howell, S., 2015. Sensitivity of seafloor bathymetry to climate-driven fluctuations in mid-ocean ridge magma supply. Science 350 (6258), 310–313. https://doi.org/10.1126/science.aad0715.

Panasiuk, S.L., Anderson, M.O., Bormann, K., Höskuldsson, Á., Martínez, F., Pałgan, D., 2025. Tectono-magmatic evolution of the Southern Reykjanes Ridge, North Atlantic, From ~11 M.y. to present. Geochem. Geophys. Geosyst. 26 (1). https://doi.org/10.1029/2024GC011847.

Parnell-Turner, R., Smith, D.K., Dziak, R.P., 2022. Hydroacoustic monitoring of seafloor spreading and transform faulting in the Equatorial Atlantic Ocean. J. Geophys. Res. Solid Earth 127 (7). https://doi.org/10.1029/2022JB024008.

Patriat, P., Sauter, D., Munschy, M., Parson, L., 1997. A survey of the Southwest Indian Ridge axis between Atlantis II Fracture Zone and the Indian Ocean triple junction: regional setting and large scale segmentation. Mar. Geophys. Res. 19 (6), 457–480. https://doi.org/10.1023/A:1004312623534.

Phipps Morgan, J., Parmentier, E.M., 1985. Causes and rate-limiting mechanisms of ridge propagation: a fracture mechanics model. J. Geophys. Res. Solid Earth 90 (B10), 8603–8612. https://doi.org/10.1029/JB090iB10p08603.

Pinzón, N., Vargas, C.A., 2021. Global variation of seismic energy release with oceanic lithosphere age. Sci. Rep. 11 (1), 601. https://doi.org/10.1038/s41598-020-80475-y.

Pitman, W.C., Larson, R.L., Herron, E.M., 1974. Magnetic lineations of the oceans, Map, 1:30000000. Geological Society of America.

Prigent, C., Warren, J.M., Kohli, A.H., Teyssier, C., 2020. Fracture-mediated deep seawater flow and mantle hydration on oceanic transform faults. Earth Planet. Sci. Lett. 532 (3), 115988. https://doi.org/10.1016/j.epsl.2019.115988.

Ren, Y., Geersen, J., Grevemeyer, I., 2022. Impact of spreading rate and age-offset on oceanic transform fault morphology. Geophys. Res. Lett. 49 (2). https://doi.org/10.1029/2021GL096170.

Resing, J.A., Lupton, J.E., Feely, R.A., Lilley, M.D., 2004. CO2 and 3He in hydrothermal plumes: implications for mid-ocean ridge CO2 flux. Earth Planet. Sci. Lett. 226 (3–4), 449–464. https://doi.org/10.1016/j.epsl.2004.07.028.

Roland, E., Behn, M.D., Hirth, G., 2010. Thermal-mechanical behavior of oceanic transform faults: implications for the spatial distribution of seismicity. Geochem. Geophys. Geosyst. 11 (7). https://doi.org/10.1029/2010GC003034.

Roth, S., Granot, R., Downey, N.J., 2019. Discrete characterization of abyssal hills: Unravelling temporal variations in crustal accretion processes at the 10°30′N segment, East Pacific Rise. Earth Planet. Sci. Lett. 525, 115762. https://doi.org/10.1016/j.epsl.2019.115762.

Rüpke, L.H., Hasenclever, J., 2017. Global rates of mantle serpentinization and H 2 production at oceanic transform faults in 3-D geodynamic models. Geophys. Res. Lett. 44 (13), 6726–6734. https://doi.org/10.1002/2017GL072893.

Ryan, W.B.F., Carbotte, S.M., Coplan, J.O., O'Hara, S., Melkonian, A., Arko, R., Weissel, R.A., Ferrini, V., Goodwillie, A., Nitsche, F., Bonczkowski, J., Zemsky, R., 2009. Global multi-resolution topography synthesis. Geochem. Geophys. Geosyst. 10 (3). https://doi.org/10.1029/2008GC002332.

Sandwell, D.T., 1986. Thermal stress and the spacings of transform faults. J. Geophys. Res. Solid Earth 91 (B6), 6405–6417. https://doi.org/10.1029/JB091iB06p06405.

Sandwell, D.T., Smith, W.H.F., 1997. Marine gravity anomaly from Geosat and ERS 1 satellite altimetry. J. Geophys. Res.: Solid Earth 102 (B5), 10039–10054. https://doi.org/10.1029/96JB03223.

Sautter, B., Escartín, J., Petersen, S., Gaina, C., Granot, R., Pubelier, M., 2024. MAPRIDGES: Global database of mid-ocean ridge segment and transform faults. SEANOE. https://doi.org/10.17882/99981.

Schierjott, J.C., Ito, G., Behn, M.D., Tian, X., Morrow, T., Kaus, B.J.P., Escartín, J., 2023. How transform fault shear influences where detachment faults form near mid-ocean ridges. Sci. Rep. 13 (1), 9259. https://doi.org/10.1038/s41598-023-35714-3.

Schouten, H., Klitgord, K.D., Whitehead, J.A., 1985. Segmentation of mid-ocean ridges. Nature 317 (6034), 225–229. https://doi.org/10.1038/317225a0.

Searle, R.C., 1983. Multiple, closely spaced transform faults in fast-slipping fracture zones. Geology 11 (10), 607. https://doi.org/10.1130/0091-7613(1983)11<607:MCSTFI>2.0.CO;2.

Sempéré, J., Macdonald, K.C., 1986. Overlapping spreading centers: implications from crack growth simulation by the displacement discontinuity method. Tectonics 5 (1), 151–163. https://doi.org/10.1029/TC005i001p00151.

Sempéré, J.-C., Purdy, G.M., Schouten, H., 1990a. Segmentation of the Mid-Atlantic Ridge between 24° N and 30°40' N. Nature 344 (6265), 427–431. https://doi.org/10.1038/344427a0.

Sempéré, J.-C., Purdy, G.M., Schouten, H., 1990b. Segmentation of the Mid-Atlantic Ridge between 24° N and 30°40' N. Nature 344 (6265), 427–431. https://doi.org/10.1038/344427a0.

Seno, T., Stein, S., Gripp, A.E., 1993. A model for the motion of the Philippine Sea Plate consistent with NUVEL-1 and geological data. J. Geophys. Res. Solid Earth 98 (B10), 17941–17948. https://doi.org/10.1029/93JB00782.

Seton, M., Müller, R.D., Zahirovic, S., Gaina, C., Torsvik, T., Shephard, G., Talsma, A., Gurnis, M., Turner, M., Maus, S., Chandler, M., 2012. Global continental and ocean basin reconstructions since 200Ma. Earth Sci. Rev. 113 (3–4), 212–270. https://doi.org/10.1016/j.earscirev.2012.03.002.

Seton, M., Müller, R.D., Zahirovic, S., Williams, S., Wright, N.M., Cannon, J., Whittaker, J.M., Matthews, K.J., McGirr, R., 2020. A global data set of present-day oceanic crustal age and seafloor spreading parameters. Geochem. Geophys. Geosyst. 21 (10), 1–15. https://doi.org/10.1029/2020GC009214.

Shaw, P.R., 1992. Ridge segmentation, faulting and crustal thickness in the Atlantic Ocean. Nature 358 (6386), 490–493. https://doi.org/10.1038/358490a0.

Shi, W., Mitchell, N.C., Kalnins, L.M., Izzeldin, A.Y., 2018. Oceanic-like axial crustal high in the central Red Sea. Tectonophysics 747–748 (April), 327–342. https://doi.org/10.1016/j.tecto.2018.10.011.

Sibrant, A.L.R., Davaille, A., Mittelstaedt, E., 2021. Rheological control on the segmentation of the mid-ocean ridges: laboratory experiments with extension initially perpendicular to the axis. Earth Planet. Sci. Lett. 557, 116706. https://doi.org/10.1016/j.epsl.2020.116706.

Simão, N., Escartín, J., Goslin, J., Haxel, J., Cannat, M., Dziak, R., 2010. Regional seismicity of the Mid-Atlantic Ridge: observations from autonomous hydrophone arrays. Geophys. J. Int. 183 (3), 1559–1578. https://doi.org/10.1111/j.1365-246X.2010.04815.x.

Sleeper, J.D., Martinez, F., 2016. Geology and kinematics of the Niuafo'ou microplate in the northern Lau Basin. J. Geophys. Res. Solid Earth 121 (7), 4852–4875. https://doi.org/10.1002/2016JB013051.

Smith, D.K., Escartín, J., Cannat, M., Tolstoy, M., Fox, C.G., Bohnenstiehl, D.R., Bazin, S., 2003. Spatial and temporal distribution of seismicity along the northern Mid-Atlantic Ridge (15°–35°N). J. Geophys. Res. Solid Earth 108 (B3). https://doi.org/10.1029/2002JB001964.

Smith, D.K., Cann, J.R., Escartín, J., 2006. Widespread active detachment faulting and core complex formation near 13° N on the Mid-Atlantic Ridge. Nature 442 (7101), 440–443. https://doi.org/10.1038/nature04950.

Spencer, S., Smith, D.K., Cann, J.R., Lin, J., McAllister, E., 1997. Structure and stability of non-transform discontinuities on the Mid-Atlantic Ridge between 24°N and 30°N. Mar. Geophys. Res. 19, 339–362. https://doi.org/10.1023/A:1004200411959.

Su, H., Liao, J., Brune, S., Gerya, T., Leng, W., 2026. Self-organization of mid-ocean ridge segments during oblique oceanisation. Commun. Earth Environ. 7 (1), 176. https://doi.org/10.1038/s43247-026-03201-y.

Taylor, B., 1979. Bismarck Sea: evolution of a back-arc basin. Geology 7 (4), 171. https://doi.org/10.1130/0091-7613(1979)7<171:BSEOAB>2.0.CO;2.

Taylor, B., Goodliffe, A.M., Martinez, F., 1999. How continents break up: Insights from Papua New Guinea. J. Geophys. Res. Solid Earth 104 (B4), 7497–7512. https://doi.org/10.1029/1998JB900115.

Thomas, M.F.H., Heine, C., van Itterbeeck, J., Ostanin, I., Seregin, A., Spaak, M., Morales, T., Essink, T.O., 2022. A new model for the evolution of oceanic transform faults based on 3D broadband seismic observations from São Tomé and Príncipe in the Eastern Gulf of Guinea. Geochem. Geophys. Geosyst. 23 (11), 1–24. https://doi.org/10.1029/2022GC010351.

Tian, X., Behn, M.D., Ito, G., Schierjott, J.C., Kaus, B.J.P., Popov, A.A., 2024. Magmatism controls global oceanic transform fault topography. Nat. Commun. 15 (1), 1914. https://doi.org/10.1038/s41467-024-46197-9.

Tsang-Hin-Sun, E., Royer, J.-Y., Perrot, J., 2016. Seismicity and active accretion processes at the ultraslow-spreading Southwest and intermediate-spreading Southeast Indian ridges from hydroacoustic data. Geophys. J. Int. 206 (2), 1232–1245. https://doi.org/10.1093/gji/ggw201.

Tucholke, B.E., Lin, J., Kleinrock, M.C., Tivey, M.A., Reed, T.B., Goff, J., Jaroslow, G.E., 1997. Segmentation and crustal structure of the western Mid-Atlantic Ridge flank, 25°25′-27°10′N and 0-29 m.y. J. Geophys. Res. Solid Earth 102 (B5), 10203–10223. https://doi.org/10.1029/96JB03896.

Tucholke, B.E., Parnell-Turner, R., Smith, D.K., 2023. The global spectrum of seafloor morphology on Mid-Ocean Ridge flanks related to magma supply. J. Geophys. Res. Solid Earth 128 (12). https://doi.org/10.1029/2023JB027367.

Tyler, S., Bull, J.M., Parson, L.M., Tuckwell, G.W., 2007. Numerical modelling of non-transform discontinuity geometry: Implications for ridge structure, volcano-tectonic fabric development and hydrothermal activity at segment ends. Earth Planet. Sci. Lett. 257 (1–2), 146–159. https://doi.org/10.1016/j.epsl.2007.02.028.

van Wijk, J.W., Blackman, D.K., 2007. Development of en echelon magmatic segments along oblique spreading ridges. Geology 35 (7), 599. https://doi.org/10.1130/G23294A.1.

Vogt, P.R., Avery, O.E., Schneider, E.D., Anderson, C.N., Bracey, D.R., 1969. Discontinuities in sea-floor spreading. Tectonophysics 8 (4–6), 285–317. https://doi.org/10.1016/0040-1951(69)90039-0.

Wetzel, L.R., Wiens, D.A., Kleinrock, M.C., 1993. Evidence from earthquakes for bookshelf faulting at large non-transform ridge offsets. Nature 362 (6417), 235–237. https://doi.org/10.1038/362235a0.

Whitehead, J.A., Dick, H.J.B., Schouten, H., 1984. A mechanism for magmatic accretion under spreading centres. Nature 312 (5990), 146–148. https://doi.org/10.1038/312146a0.

Wilson, D.S., 1990. Kinematics of overlapping rift propagation with cyclic rift failure. Earth Planet. Sci. Lett. 96, 384–392.

Wolfson-Schwehr, M., Boettcher, M.S., 2019. Global characteristics of oceanic transform fault structure and seismicity. In: Transform Plate Boundaries and Fracture Zones. Elsevier, pp. 21–59.

Zhang, T., Gordon, R.G., Wang, C., 2018. Oblique seafloor spreading across intermediate and superfast spreading centers. Earth Planet. Sci. Lett. 495, 146–156. https://doi.org/10.1016/j.epsl.2018.05.001.

Zheng, T., Lin, J., Zhong, Q., 2022. Spreading-rate dependence of hydroacoustic and teleseismic seismicity of ridge-transform systems: East Pacific Rise, Galapagos Ridge, and Mid-Atlantic Ridge. Acta Oceanol. Sin. 41 (5), 122–133. https://doi.org/10.1007/s13131-021-1936-6.